THE PREDICTIVE CAPABILITY OF FAILURE MODE CONCEPT - BASED STRENGTH CONDITIONS FOR LAMINATES COMPOSED OF UD LAMINAE UNDER STATIC TRI-AXIAL STRESS STATES

R. Cuntze
formerly MAN Technologie AG, Augsburg, Germany
D-85229 Markt Indersdorf, Germany. Tel.: 0049 8136 7754, Ralf_ Cuntze@t-online.de

Abstract

This paper represents the author's contribution to the Second World-Wide Failure Exercise (WWFE-II) using his Failure Mode Concept (FMC) modelling capability. The WWFE-II deals with the behaviour of isotropic material and unidirectional (UD) as well as multi-directional UD laminae-composed laminates subjected to three dimensional (tri-axial) states of stress. 12 challenging Test Cases were provided by the organisers and those covered stress-strain curves and failure envelopes under 3D stress states. The application of the new FMC model has extended the modelling from 2D into 3D situations and has taken into account the effect of hydrostatic pressure and 2nd glass temperature shift factor on the stress strain curves and failure envelopes. The FMC model was capable of successfully solving the majority of all the problems and a comparison between the predictions and test data is planned to be published in Part B of the WWFE-II.

Keywords: FMC, failure criteria, multi-axial, hydrostatic compression, triaxial.

Nomenclature

a_s, b_s	Parameters in softening regime
a_1, a_2, a_3	Fitting parameters for 2ndTg effect
$b_{\perp}^{\tau}, b_{\perp\|\|}$	UD material's internal 'friction parameters' of the FMC-based model
$E_1 = E_{\|\|}$, $E_2 = E_3 = E_{\perp}$	Elastic moduli of a UD lamina in the directions $x_1 \equiv 1 = \|\|$, $x_2 \equiv \perp$, $x_3 \equiv \perp$,
E_0	Initial Young's modulus
E_{sec}	Secant elasticity modulus
Eff	Resultant (global) stress effort of all interacting failure modes
Eff^{mode}	Stress effort of a UD-lamina in a distinct failure mode
$E_{\|\|f}$	Elastic filament (fibre) modulus in fibre (x_1) direction
$E\perp f$	Elastic filament (fibre) modulus transversal to fibre direction
$e_{\|\|}^{t}, e_{\|\|}^{c}$	Tensile and compressive failure strain of a UD-lamina in x_1 direction
$F_{\|\|}^{\sigma}, F_{\|\|}^{\tau}, F_{\perp}^{\sigma}, F_{\perp}^{\tau}, F_{\perp\|\|}$	Failure functions for FF and IFF modes
F_{2ndTg}	Reduction factor or function to consider the 2ndTg effect
G_{12} ; G_{23}	Shear modulus of a UD lamina in the x_1-x_2 plane ($\equiv G_{\|\|\perp}$); in the x_3-x_2 plane ($\equiv G_{\perp\perp}$)
$G_{12,sec}$	secant shear modulus in the x_1-x_2 plane
I_1, I_2, I_3, I_4, I_5	Invariants of the transversely-isotropic UD-material
I_1, J_2	Invariants of the isotropic matrix material
M	Matrix weakening exponent
m	Mode interaction or rounding-off exponent
N	Repetitions of sub-laminates, Ramberg-Osgood exponent
P	Pressure on the faces of the specimen (absolute value)
p_{hyd}	Hydrostatic pressure (absolute value)
$\overline{R}$, R	Average measured strength, strength design allowable for Design Verification (an A- or a B-value)
$R_{p0.2}$, $R_{c0.2}$	Tensile, compressive stress values at 0.2 % plastic strain ≡ yield strength ($R_{0.2}$ denotes both properties)
R_{τ}	Cohesive strength of a ductile behaving material
$R_{\|\|f}$	Strength of the filament (fibre)
$R_{\|\|}^{t} \equiv X^{t}, R_{\|\|}^{c} \equiv X^{c}$	UD tensile and compressive strength parallel to the fibre direction
$R_{\perp}^{t} \equiv Y^{t}, R_{\perp}^{c} \equiv Y^{c}$	UD tensile and compressive strength transverse to the fibre direction
$R_{\perp\|\|} \equiv S$:	UD in-plane shear strength, transverse/parallel to the fibre direction
$[S]$	Compliance matrix
T_g	Glass transition temperature
Tr	Definition for the Triaxiality value $Tr = (I_1/3)/\sqrt{3J_2} = \sigma_m / \sigma_{eq}^{Mises}$, $\sigma_{eq}^{Mises} = \sqrt{3J_2}$ or in Lode coordinates $Tr = \left[\sqrt{2}/3\right] \cdot (I_1/\sqrt{3})/\sqrt{2J_2}$ uniaxial: $Tr = 1/3$
t	Thickness of the laminate
V_f	Fibre volume fraction
x_1, x_2, x_3	Coordinates of the UD lamina (x_1 = fibre direction ‖, x_2 = direction

	transverse to the fibre $\perp$, x_3 = thickness direction)
ε_1, ε_2, ε_3	Normal strains of a UD lamina
η	Degradation function in softening regime
$\gamma_{12} = \gamma_{21}$; $\gamma_{13} = \gamma_{31}$; $\gamma_{23} = \gamma_{32}$	Shear strains of a UD lamina
ν_{12}	Major Poisson's ratio in the WWFE-II ($\equiv \nu_{\perp\parallel}$ in VDI 2014)
$\nu_{\perp\perp}$	Poisson's ratio in the transversal plane ($\equiv \nu_{23}$)
Φ	Parameter which represents the 120°-symmetry of brittle isotropic materials
Θ_{fp}	Designation of the fracture plane angle
μ	Internal friction coefficient of the isotropic material
$\mu_{\perp\parallel}, \mu_{\perp\perp}$	Internal friction coefficients of the transversely-isotropic material model
σ_{ef}	Effective hydrostatic stress in the constrained matrix material (absolute value)
σ_{hyd}	Hydrostatic stress (sign dependent)
σ_1, σ_2, σ_3	Normal stresses in a UD lamina
σ_I, σ_{II}, σ_{III}	Principal stresses in an isotropic material
σ_2^c, σ_1^t	Compressive stress across and tensile stress along the fibre direction
$\sigma_{\parallel}$, $\sigma_{\perp}$	Stresses parallel and transverse to the fibre direction (symbolic denotation)
$\hat{\sigma}_x, \hat{\sigma}_y$	Average in-plane stresses of the laminate
σ_{eq}^{mode}	Equivalent stresses of a mode ($\sigma_{eq}^{\parallel\sigma}, \sigma_{eq}^{\parallel\tau}, \sigma_{eq}^{\perp\sigma}, \sigma_{eq}^{\perp\tau}, \sigma_{eq}^{\perp\parallel}$) which include load-induced mechanical stresses and residual stresses
σ_{1f}, σ_{2f}	Filament stress in x_1 direction; in x_2 direction
$\{\sigma\}$	Stress vector of the lamina
$\hat{\sigma}$	Average stress loading a laminate's face or cross section
$\tau_{12} = \tau_{21}$, $\tau_{13} = \tau_{31}$, $\tau_{23} = \tau_{32}$	Associated shear stresses of a UD lamina
$\tau_{\perp\parallel}, \tau_{\perp\perp}$	Shear stresses transverse/parallel and transverse/transverse to the fibre direction
Abbreviations	
CLT	Classical Laminate Theory
CDS	Characteristic Damage State
CDM	Continuum Damage Mechanics
CrF	Crushing Fracture
CTE	Coefficient of thermal expansion
CME	Coefficient of moisture expansion
F	Failure function
FEA	Finite Element Analysis
FF, IFF	Fibre Failure, Inter-Fibre Failure
FMC	Failure Mode Concept
FRP	Fibre-Reinforced Plastic
MfFD	Multifold Failure Domain
MiFD	Mixed Failure Domain (interaction of several failure modes)
NF, SF	Normal fracture, shear fracture
UD	Uni-directional

wrt	with respect to
Subscripts, superscripts, and signs	
$_{c, t}$	Compressive, tensile (German Guideline VDI 2014)
$_{cr}$	Critical
$_{eq}$	Equivalent
$_{ef}$	Effective hydrostatic stress and effective temperature difference at curing (stress free temperature – room temperature)
$_{f, m}$	Fibre (or filament), matrix
$_{fr}$	Fracture
$_{fp}$	Fibre parallel fracture plane
hard	Hardening
$_{hyd}$	Hydrostatic
k	k^{th} lamina
$_{L, R}$	Denotes stress from external applied load, residual stress
n, t	Normal, tangential to the fibre plane of the UD lamina
$_{ns}$	n-fold symmetric lay-up
$_{p, ps}$	Principal (in §2.2.1), pseudo (in §2.3.1)
$_{p0.2}$	Tensile yield strength
Res	Reserve
soft	Softening
$_{s}$	Symmetric lay-up
$_{trf}$	Trigger factor
$_{\tau, \sigma}$	Failure either induced by Mohr's shear or by Mohr's normal stress acting at the physical fracture plane
$_{\perp, \parallel}$	Transverse, parallel to fibre direction of a UD lamina
$_{0.2}$	0.2 remaining plastic strain (technical onset of yielding)
1, 2, 3	directions in the UD lamina
I, II, III	Principal stresses in an isotropic material
x, y, z	Directions in the laminate
$\bar{}$	Typical or average (sometimes the statistical mean) needed when modelling
^	over the thickness smeared (averaged)
$_{\perp\perp}$	Designation of transverse plane (as subscript and superscript).

1. Introduction

Tri-axial failure states are encountered in thick structures such as submarines, in bolted and screwed joints, bearings (such as sealed polymer bearing cartridges pressurized up to 600 MPa), impact and ballistics, and in other applications like composite high pressure vessels. However, progress for understanding failure under 3D stresses has been limited as the majority of previous investigations have focused on testing under bi-axial and tri-axial compression (such as hydrostatic pressure loading) and little effort has been made on developing mature and accurate theories. Consequently, there is a strong need to validate and benchmark failure conditions under 3D stresses, including the compression domain.

Basically, high pressure and especially high hydrostatic pressure are likely to have several effects. Firstly, it 'heals flaws' and increases stiffness and strength but the final failure behaviour becomes more brittle (sudden fracture, damage tolerance capability of the structure is reduced). Secondly, it elasto-mechanically 'strengthens' the compressed UD solid. Thirdly, it causes at high pressures a weakening of the matrix with a following reduction of the UD material's stiffness and strength. Therefore, the effective 'local' hydrostatic pressure in the matrix has to be taken into the consideration of the latter effect.

It is recognised that, from an industrial point of view, a designer has to consider static and cyclic loadings. However, failure theories under static loading have posed a real challenge to industry and academia alike, Refs[1,2]. The author has developed a model, known as the **F**ailure **M**ode **C**oncept (FMC) model, Refs[3,4,5,6], that may be used in design and the model was validated and benchmarked as a part of a previous activity, called the World-Wide Failure Exercise. Refs[1,2]. The challenges that were addressed in that exercise wee all related to the accuracy of the failure criteria under 2D stresses, i.e. under in-plane loading. The author's model was ranked to be one of the mature methods.

In order to understand the predictive capability of a wide range of failure criteria for use under 3D stresses, a new activity, called ‘the second world-wide failure exercise (WWFE-II), was organised, Refs[7,8]. In this exercise, the challenges include accurate prediction of 12 Test Cases that include various materials (polymer, carbon and glass fibres, different epoxy matrices), various stacking sequences, a wide range of loading conditions involving uni-axial and bi-axial tension and compression, torsion shear, hydrostatic loading as well as through-thickness stresses.

This paper describes a new development of the FMC model and its application to solve the test problems of the WWFE-II.

2. Formulation of the FMC theory

A failure condition is the mathematical formulation of a failure curve or a failure surface, respectively. Existing failure conditions often map a course of multi-axial test data by one *global* equation, such as Equation (1). These do not often consider whether the data belongs to one or more failure mechanisms or failure modes. Also, the strength and failure behviour in one quadrant (e.g. compression-compression) is usually affected by the strengths under other loadings (e.g. uniaxial tension), In other words, if a correction or change in the domain of one failure mode has to be made this usually affects the domain of another independent mode. This is a mathematical but physically questionable consequence.

In order to avoid the use of a single equation to describe the failure, using a 'global fitting', the author introduced a 'failure mode-related fitting' which then, however, will require a failure condition for each mode, Equation (2),

$$1\ global\ \text{failure condition}: \quad F(\{\sigma\}, \{R\}) = 1 \ \text{(usual formulation)}, \tag{1}$$

$$\text{a } set \text{ of } mode \text{ failure conditions}: \quad F(\{\sigma\}, R^{mode}) = 1 \ \text{(FMC principle)}. \tag{2}$$

Such a set of mode failure conditions will build up, in a piecewise manner, the multi-dimensional failure surface and also the failure curve. Fracture is understood in this paper as a separation of material. The material is assumed to be initially free of damage such as technical cracks (size in the order of mm) and delaminations but not free of small flaws (size in the order of microns) prior to loading. Types of fracture which are recognised by fractography in case of pore-free ('dense') transversely-isotropic ideal UD materials are brittle fracture failure (Normal Fracture (NF) ≡cleavage) and shear fracture (SF) failure under compression.

2.1. Fundamentals on stresses, strengths, invariants and micro-mechanics

For a UD material element, the 3D state of stress $\{\sigma\} = (\sigma_1, \sigma_2, \sigma_3, \tau_{23}, \tau_{31}, \tau_{21})^T$ is normally

encountered as shown in **Fig. 1**. Because of the symmetries of the transversely-isotropic UD material, modelled an ideal crystal, there are 5 basic strengths and 5 elasticity properties, only. Therefore, the characterisation of the strength requires the measurement of five independent basic lamina strengths, Ref[9]:

$R_{\parallel}^{t}\,(=X^{t})$ and $R_{\parallel}^{c}\,(=X^{c})$ as tensile and compression strength parallel to the fibres.

$R_{\perp}^{t}\,(=Y^{t})$ and $R_{\perp}^{c}\,(=Y^{c})$ as tensile and compressive strength transversal to the fibre direction), and

$R_{\perp\parallel}\;(=S)$ as in-plane shear strength.

Strength criteria (F < = >1) or failure conditions (F = 1) should be formulated by invariants based on the macro-mechanical UD-stresses, see Fig. 1. Their application is advantageous for an optimal formulation of so-called *scalar* Failure Conditions. According to Ref[11], in general, failure conditions can be at most a function of the stress invariants under the rotation of the x_2, x_3 -axes around the x_1-axis or fibre axis, respectively.

The material symmetry-based UD invariants (I_4, I_5 from [10]) used in the FMC are:

$$I_1 = \sigma_1\,, \qquad I_2 = \sigma_2 + \sigma_3\,,$$

$$I_3 = \tau_{31}^2 + \tau_{21}^2\,, \qquad I_4 = (\sigma_2 - \sigma_3)^2 + 4\tau_{23}^2\,, \tag{3a-e}$$

$$I_5 = (\sigma_2 - \sigma_3)(\tau_{31}^2 - \tau_{21}^2) - 4\tau_{23}\tau_{31}\tau_{21}\,.$$

Fig. 2 defines the positive angle of fibre orientation in each lamina.

2.1.2. Stress-strain relationship and micro-mechanical formulae

The stress-strain relationship reads, following [9],

$$\{\varepsilon\} = [S]\,\{\sigma\} \tag{4}$$

For imposing pressure-related effects on the matrix and in consequence on the UD material micromechanical formulas had to be applied together with the data. The following equations were employed, Ref [9]:

$$E_{\parallel} = E_{\parallel f} \cdot V_f + E_m \cdot (1 - V_f) \cong E_f \cdot V_f ,$$

$$E_{\perp} = \frac{E_m}{1 - \nu_m^{\,2}} \cdot \frac{1 + 0.85 \cdot V_f^{\,2}}{(1 - V_f)^{1.25} + V_f \cdot E_m / (E_{\perp f} \cdot (1 - \nu_m^{\,2}))} \quad , \qquad \text{(5a-d)}$$

$$G_{\perp\parallel} = \frac{G_m \cdot (1 + 0.4 \cdot V_f^{\,0.5})}{(1 - V_f)^{1.5} + V_f \cdot G_m / G_{\perp\parallel f}} ,$$

$$\nu_{\perp\parallel} = \nu_{\perp\parallel f} \cdot V_f + \nu_m \cdot (1 - V_f) ,$$

with $G_m = E_m / (2 + 2 \cdot \nu_m)$. Equation (5) may be used for the regime $0.3 \le V_f \le 0.65$.

2.2. FMC-based failure conditions and their interaction

2.2.1 Derivation of failure conditions

In total, 5 strengths and 2 material friction-related parameters will be necessary when applying FMC-based UD failure conditions. The following set of failure functions *F* is applied on a lamina level:

$$FF1: \quad F_{||}^{\sigma} = \frac{I_1}{\bar{R}_{||}^{t}} \quad , \qquad FF2: \quad F_{||}^{\tau} = \frac{-I_1}{\bar{R}_{||}^{c}} \quad ,$$

$$IFF\ 1: \quad F_{\perp}^{\sigma} = \frac{I_2 + \sqrt{I_4}}{2\bar{R}_{\perp}^{t}} \quad , \quad IFF\ 2: \quad F_{\perp}^{\tau} = (b_{\perp}^{\tau} - 1)\frac{I_2}{\bar{R}_{\perp}^{c}} + \frac{b_{\perp}^{\tau}\sqrt{I_4}}{\bar{R}_{\perp}^{c}} \quad , \qquad \text{(6a-e)}$$

$$IFF\ 3: \quad F_{\perp||} = \frac{I_3^{3/2}}{\bar{R}_{\perp||}^{\,3}} + b_{\perp||}\frac{I_2 \cdot I_3 - I_5}{\bar{R}_{\perp||}^{\,3}} \quad .$$

Furthermore, as abbreviation $I_2 \cdot I_3 - I_5 = I_{23-5}$ will be used.

The superscripts ^{t}, ^{c} stand for tensile, compressive. The superscripts $^{\sigma}$ and $^{\tau}$ mark the type of fracture failure whether it is caused by a tensile stress σ (NF) or a shear stress τ (SF), e.g. due to a compressive normal stress $\sigma_{||}^{c}$ or a transverse normal stress $\sigma_{\perp}^{c}$. Whether a failure may be called a SF or a NF, depends on the envisaged size scale. An example is IFF2: It is macro-mechanically a SF and micro-mechanically a NF of the matrix.

2.2.2. Determination of the friction-related b-parameters

In addition to the five strength values, Equation (6) indicate that two friction-related model parameters ($b_{\perp\|}$, $b_{\perp}^{\tau}$) are needed for the analysis, These are normally obtained from curve fitting of multi-axial test data. For IFF2, a fracture angle measured in the uni-axial $R_{\perp}^{c}$ compression test may be alternatively employed.

As a simplifying procedure, one statistically based calibration point for each of the two modes delivers, after inserting its coordinates into the IFF conditions (for $F_{\perp\|}$ from a point $\left(\sigma_{2}^{\ c}, \tau_{21}^{\perp\|}\right)$, see [3,4], and for $F_{\perp}^{\tau}$ from ($\sigma_{2}^{c\tau}, \sigma_{3}^{c\tau}$)), and after a resolving the two failure conditions of Equation (6), namely $F_{\perp||} = 1$ and $F_{\perp}^{\tau} = 1$ the determining equations for the b-parameters

$$b_{\perp||} = \frac{\overline{R}_{\perp||}^{\ 4} - \tau_{21}^{\perp||4}}{2\sigma_{2}^{c\perp||} \cdot \tau_{21}^{\perp||2} \cdot \overline{R}_{\perp||}} \quad \text{and} \quad b_{\perp}^{\tau} = \frac{1 + (\sigma_{2}^{c\tau} + \sigma_{3}^{c\tau}) / \overline{R}_{\perp}^{c}}{(\sigma_{2}^{c\tau} + \sigma_{3}^{c\tau}) / \overline{R}_{\perp}^{c} + \sqrt{(\sigma_{2}^{c\tau} - \sigma_{3}^{c\tau})^{2}} / \overline{R}_{\perp}^{c}} . \quad (7, 8)$$

2.2.3. New developments in the FMC theory since WWFE-I

A modification of one IFF condition was made in Ref[6] to replace the so-called ‘in-plane shear failure mode condition IFF3’ by a numerically advantageous formulation. In that paper, a very satisfying semi-validation of the 3D IFF3 condition, reduced to 2D, could be achieved when judging it versus the 2D experiments provided by the WWFE-I and other sources.

The reason was a numerical problem in the ‘old’ formulation that probably no intersection is

achieved of the applied stress vector with the mode curve IFF3.

The numerical problem above is just a problem of the mode interaction zone (see section on mode interaction). Instead of a query it can be bypassed when, at first, for $F_{\perp||}$ the usual *principle of proportional stressing* (all stresses of the actually given state of stress or stress vector are equally factored) is abandoned, that interprets so-called mode reserve factors as mode stretch factors of the actual stress vector. This stretching ends when the associated mode failure curve is met.

So, when establishing the interaction zone, the description can be modified if the physical basement is not violated, I_{23-5} is kept in order to describe the different physical effects of σ_2 and σ_3 in the possible combinations with shear stresses. Now, instead of factoring the full state of stress in Equation (9), that means factoring each single stress in the invariants used, just the mode driving shear stress(es) τ_{21},τ_{31} is(are) factored. And not for instance the shear stress τ_{23} (has a normal stress effect; remind transformation).

Unfortunately, with this approach the failure condition includes a reserve factor with power 2 and 3

$$\frac{I_3^{3/2}\cdot f_{Res}^{\perp||\,3}}{\overline{R}_{\perp||}^{\;3}}+b_{\perp||}\frac{I_{23-5}\cdot f_{Res}^{\perp||\,2}}{\overline{R}_{\perp||}^{\;3}}=\;1 \qquad (9)$$

with f_{Res}^{mode} as reserve factor of the IFF3 mode.

The determination of a mode reserve factor requires the solution of an unpleasant third order equation. Therefore, the approach for establishing the interaction domain will be modified in order to obtain the numerical advantageous powers 4 and 2

$$\frac{I_3^{\,2}\cdot f_{Res}^{\perp\|\,4}}{\overline{R}_{\perp\|}^{\,4}} + b_{\perp\|}\frac{I_{23-5}\cdot f_{Res}^{\perp\|\,2}}{\overline{R}_{\perp\|}^{\,3}} = 1 \ . \qquad (10)$$

Of course, the parameter $b_{\perp\|}$ is now slightly different to the former one. The rationale behind the creation of Equation (10) is that this procedure has no effect because this condition is used then instead of Equation (6e) as the new mapping function or curve fitting function, respectively.

The procedure takes the former unpleasant non-intersection problem completely away. In comparison to WWFE-I no queries are necessary anymore, just a quadratic equation needs to be solved now.

As it is a measure, which is also applicable in linear and non-linear analysis and which is more advantageous for the coming investigations, a more general quantity shall be introduced. It is the so-called 'mode stress effort' which has the advantage that it is always material-based and can be applied for linear and nonlinear analyses. Especially in the case of residual stresses instead of a material-based reserve factor *f* a material stress effort *Eff* (linearly: inverse of *f*) is employed, see section 2.2.5 .

2.2.4. Limit of macro-mechanical fibre failure descriptions

In general, the fibre failure mode FF1 (and *FF2*) cannot be described by a homogenized (smeared) macro-mechanical stress value σ_1. Thus, the engineering-like macro-mechanical modelling has to be replaced by an accurate micro-mechanical one, Ref[3], as:

$$FF1\text{: } F_{\|}^{\sigma} : I_1 = \sigma_1 \ \approx \ V_f \cdot \sigma_{1f} \ = V_f \cdot \varepsilon_1 \cdot E_{1f} = \ \varepsilon_1 \cdot E_{\|} \qquad (11)$$

Where ε_1 macro-mechanical strain and σ_{1f} tensile filament (fibre) stress which is proportional to the strain and responsible for fracture.

Above reformulation, Equation (11), is necessary if multi-axial compression is applied which means that the Poisson effect is active and if FF1 may occur even in case of zero applied external stress σ_1 because bi-axial compression may cause fibre fracture.

2.2.5. Stress effort of modes and corresponding equivalent stress

The stress effort of each mode is derived by resolving the equations:

$$\frac{[\sigma_1]/Eff^{||\sigma}}{\bar{R}_{||}^{t}}=1\ ,\quad \frac{[-\sigma_1]/Eff^{||\tau}}{\bar{R}_{||}^{c}}=1\ ,$$

$$\frac{[(\sigma_2+\sigma_3)+\left|\sqrt{(\sigma_2-\sigma_3)^2+4\cdot\tau_{23}{}^2}\right|]/Eff^{\perp\sigma}}{2\bar{R}_{\perp}^{t}}=1\ , \qquad \text{(12a-e)}$$

$$\frac{[b_{\perp}^{\tau}\cdot\sqrt{(\sigma_2-\sigma_3)^2+4\cdot\tau_{23}{}^2}+(b_{\perp}^{\tau}-1)\cdot(\sigma_2+\sigma_3)]/Eff^{\perp\tau}}{\bar{R}_{\perp}^{c}}=1\ ,$$

$$\frac{(\tau_{31}^2+\tau_{21}^2)^2}{Eff_{\perp||}^{4}\cdot\bar{R}_{\perp||}^{4}}+b_{\perp||}\frac{2\sigma_2\cdot\tau_{21}^2+2\sigma_3\cdot\tau_{31}^2+4\tau_{23}\tau_{31}\tau_{21}}{Eff_{\perp||}^{2}\cdot\bar{R}_{\perp||}^{3}}=\ 1$$

for the respective effort.

An equivalent stress σ_{eq} is always positive such as the strength. It includes all actual load stresses and the residual stresses (from curing etc.) that are acting together in a given mode. The vector of the modes' equivalent stresses reads

$$\left\{\sigma_{eq}^{mode}\right\}=\left(\sigma_{eq}^{||\sigma}\ ,\ \sigma_{eq}^{||\tau}\ ,\ \sigma_{eq}^{\perp\sigma}\ ,\ \sigma_{eq}^{\perp\tau}\ ,\ \sigma_{eq}^{||\perp}\right)^T\ . \qquad (13)$$

Employing the mode *strength* $\bar{R}^{mode}$, its *equivalent stress* σ_{eq}^{mode}, and Equation (13) - according to the general equation $Eff^{mode} = \sigma_{eq}^{mode} / \bar{R}^{mode}$ - the following set of formulas is given:

FF 1 $Eff^{\parallel\sigma} = \sigma_1 / \bar{R}_{\parallel}^{t} = \sigma_{eq}^{\parallel\sigma} / \bar{R}_{\parallel}^{t}$ with $\sigma_1 \cong \varepsilon_1^t \cdot E_{\parallel}$,

FF 2 $Eff^{\parallel\tau} = -\sigma_1 / \bar{R}_{\parallel}^{c} = +\sigma_{eq}^{\parallel\tau} / \bar{R}_{\parallel}^{c}$ with $\sigma_1 \cong \varepsilon_1^c \cdot E_{\parallel}$, (14a-e)

IFF 1 $Eff^{\perp\sigma} = [(\sigma_2 + \sigma_3) + \sqrt{\sigma_2^{\,2} - 2\sigma_2 \cdot \sigma_3 + \sigma_3^{\,2} + 4\tau_{23}^{\,2}}\,] / 2\bar{R}_{\perp}^{t} = \sigma_{eq}^{\perp\sigma} / \bar{R}_{\perp}^{t}$,

IFF 2 $Eff^{\perp\tau} = [(b_{\perp}^{\tau} - 1)\cdot(\sigma_2 + \sigma_3) + b_{\perp}^{\tau}\sqrt{\sigma_2^{\,2} - 2\sigma_2\sigma_3 + \sigma_3^{\,2} + 4\tau_{23}^{\,2}}\,] / \bar{R}_{\perp}^{c} = +\sigma_{eq}^{\perp\tau} / \bar{R}_{\perp}^{c}$

IFF 3 $Eff^{\perp\parallel} = \{[b_{\perp\parallel} \cdot I_{23-5} + (\sqrt{b_{\perp\parallel}^{\,2} \cdot I_{23-5}^{\,2} + 4 \cdot \bar{R}_{\perp\parallel}^{\,2} \cdot (\tau_{31}^2 + \tau_{21}^2)^2}\,]/(2 \cdot \bar{R}_{\perp\parallel}^{\,3})\}^{0.5} = \sigma_{eq}^{\perp\parallel} / \bar{R}_{\perp\parallel}$

with $I_{23-5} = 2\sigma_2 \cdot \tau_{21}^2 + 2\sigma_3 \cdot \tau_{31}^2 + 4\tau_{23}\tau_{31}\tau_{21}$. (15)

Above stresses include the nonlinearly load-dependent load stresses $\{\sigma\}_L$ and the equally nonlinearity dependent residual stresses $\{\sigma\}_R$.

Note: 1) Each failure mechanism is affected by an associated typical stress state. The failure mechanism with the highest stress effort will dominate the failure. The mode effort has to become zero if the mode driving stress is zero!. 2) Due to IFF the curing stresses decay in parallel to the degradation. 3) The not design driving stresses of a mode might increase or decrease the stress effort of the design driving one. This is pronounced by σ_{eq}. *4) Not a Mises equivalent stress exists only). There are others, too.*

2.2.6. Interaction of failure modes

Due to the fact that the full failure surface consists of five parts, an interaction of these partial

surfaces has to be executed. Cuntze models these failure mode interactions by a simple probabilistically based 'series spring model' approach [3]. Such a model describes the lamina failure system as a series failure system which fails whenever any of its elements fails. Each mode is one element of the failure system and is seen to be independent of the others.

By this method, the interaction between FF and IFF modes as well as between the various IFF modes acts - in these 'mixed' failure domains - as a rounding-off procedure linked to the determination of the desired values for the resultant stress effort Eff. This effort automatically takes into account the interactions between all the affected modes by summing up all the proportionate mode stress efforts according to Equation (16)

$$Eff^{m} = \sum_{1}^{5} (Eff^{modes})^{m} = (Eff^{mode\,1})^{m} + (Eff^{mode\,2})^{m} + ... + .. \quad \text{in general} \quad (16a,b)$$

$$Eff^{m} = (Eff^{\parallel\sigma})^{m} + (Eff^{\parallel\tau})^{m} + (Eff^{\perp\sigma})^{m} + (Eff^{\perp\tau})^{m} + (Eff^{\perp\parallel})^{m} \qquad \text{for UD}$$

$$= 1 = 100\% \text{ , if failure.}$$

In other words, the interaction equation includes all mode stress efforts and each of them represents a portion of load-carrying capacity of the material. In practice in thin laminae, at maximum, 3 modes of the 5 modes will physically interact. Considering 3D-loaded thick laminae, there, all 3 IFF modes might interact.

For the application of the Equation (16) a value for the interaction exponent m is usually obtained by curve fitting of test data in the interaction zone. Author's experience shows $2.5 < m < 3$, e.g. for CFRP. The mode interaction exponent m is also termed rounding-off exponent, the size of which is high in case of low scatter and vice versa. As a simplifying engineering assumption, m is always given the same value, regardless of the distinct mode interaction domain! As with other interaction equations also for m it is valid: a lower value chosen for the interaction exponent is more on the safe side.

Of interest is not only the interaction of the fracture surface parts in the discussed mixed failure domains or interaction zones of adjacent failure modes, respectively, but further failure in a multi-fold failure domain (superscript $^{\mathrm{MfFD}}$) such as in the (σ_2^t, σ_3^t)-domain. Here, the associated mode stress effort acts twofold. It activates failure in two directions and may be engineering-like considered by adding a multi-fold failure term, proposed by Awaji [3] for isotropic materials, which can be applied to UD material in the transversal (quasi-isotropic) plane as well

$$Eff^{\,m} = ... + ... + ... + ... + (Eff^{\perp\sigma})^m + (Eff_{\perp}^{MfFD})^m \qquad (17)$$

with $Eff_{\perp}^{MfFD} = (\sigma_2^t + \sigma_3^t)/2R_{\perp}^{tt}$, $R_{\perp}^{tt} \approx R_{\perp}^{t}/\sqrt[m]{2}$.

Equation (17) practically represents a biaxial tensile strength $R_{\perp}^{tt}$. The effect above, denoted joint failure probability, is inherent in brittle materials. The development of the oriented flaws and their growth is driven by across acting principle stresses in 3D states of stress. This is valid in a 2D manner for UD material consisting of the usual matrix materials: in the $\perp\perp$-plane the UD principal stresses act perpendicular to the fibre direction and both stresses σ_2 and σ_3 have statistically the same effect under tensile loading.

All mode efforts have been inserted Into Equation (16) in order to practically have the full set of conditions in just one equation combined during the numerical analysis instead of dealing with each single failure condition. However, when automatically inserting the FEA stress output $\{\sigma\}=(\sigma_1,\sigma_2,\sigma_3,\tau_{23},\tau_{13},\tau_{12})^T$ into all 5 effort equations some efforts may become negative which mechanically means zero effort. One can solve this problem by using the absolute values of the several parts of the envisaged failure condition as follows.

$$Eff^{m} = \left(\frac{(\sigma_1 + |\sigma_1|)}{2\overline{R}_{\parallel}^{t}}\right)^{m} + \left(\frac{-\sigma_1 + |\sigma_1|}{2\overline{R}_{\parallel}^{c}}\right)^{m} + \left(\frac{\sigma_2 + |\sigma_2|}{2\overline{R}_{\perp}^{t}}\right)^{m} + \left(\frac{|\tau_{21}|}{\overline{R}_{\perp\parallel}} \cdot \sqrt{R2D}\right)^{m/2} + \left(\frac{-\sigma_2 + |\sigma_2|}{2\overline{R}_{\perp}^{c}}\right)^{m}, \qquad (18a)$$

with the radicand $R2D = b_{\perp\parallel} \cdot \sigma_2 + \sqrt{(b_{\perp\parallel} \cdot \sigma_2)^2 + R_{\perp\parallel}^{\ 2}}$.

Equation (18a) is obtained after inserting $\{\sigma\}=(\sigma_1,\sigma_2,\tau_{12})^T$ into Equation (14) and then summing up the single portions. Equation (18a) is obtained after inserting $\{\sigma\}=(\sigma_1,\sigma_2,\tau_{12})^T$ into Equation (14) and then summing up the single portions. A non-positive mode effort (means: no failure danger) is automatically sorted out by this procedure.

Instead of applying the procedure above one may also formalistically take the Macauly brackets (≡ Föppl symbols). They describe a discontinuous function and are defined here by

$$\left\{Eff^{mode}\right\} = \begin{cases} 0\ , & Eff^{mode} < 0 \\ Eff^{mode}, & Eff^{mode} \geq 0 \end{cases}.$$

For completion, the 3D formulation of Equation (16b) is given again (for the *Eff*s see Equations (14))

$$Eff^{m} = \left(Eff^{\parallel\sigma}\right)^{m} + \left(Eff^{\parallel\tau}\right)^{m} + \left(Eff^{\perp\sigma}\right)^{m} + \left(Eff^{\perp\tau}\right)^{m} + \left(Eff^{\perp\parallel}\right)^{m}. \qquad (18b)$$

This equation can be developed similarly to Equation (18a) and written.

2.2.7. Failure conditions for delamination

Delamination conditions are just a *subset* of the FMC conditions set and are thereby captured by the Equations (14). They are given here in a separate manner because other researchers present special delamination conditions.

With regard to the 3D nature of the IFF conditions, both, IFF1 ($F_{\perp}^{\sigma}$:= transverse tensile failure; inter-laminar stresses $\sigma_3^t, \tau_{32}, \tau_{31}$ may cause cracking) and IFF2 ($F_{\perp}^{\tau}$:= wedge failure; intra-laminar stresses such as σ_2^c, τ_{21} cause cracking and may initiate a local 3D state of stress activaing σ_3) can also serve as conditions for the assessment of *'onset of delamination'* which is – in general – called *laminate* failure. One or two modes will be the design driving ones in the critical local 'material' point of a composite lay-up. These are activated by the delamination-critical stress state $\{\sigma\}_{lamina} = (0, \sigma_2, \sigma_3^t, \tau_{23}, \tau_{31}, \tau_{21})^T$ that includes all interlaminar stresses. Introducing the two relevant combinations of the delamination-active stress vector above into the Equations (14) delivers:

Tension/shear stressing

$$(Eff^{\perp\sigma})^m + (Eff^{\perp\parallel})^m = 1 \qquad \text{with} \quad \{\sigma\}_{lamina} = (0, \sigma_2^t, \sigma_3^t, \tau_{23}, \tau_{31}, \tau_{21})^T, \quad (19a)$$

Compression/shear stressing

$$(Eff^{\perp\tau})^m + (Eff^{\perp\parallel})^m = 1 \qquad \text{with} \quad \{\sigma\}_{lamina} = (0, \sigma_2^c, \sigma_3^c, \tau_{23}, \tau_{31}, \tau_{21})^T, \quad (19b)$$

and interacted, when necessary. For engineering reasons, the interaction exponent *m* is chosen the same as before.

2.3. Investigation of the pressure effect

2.3.1. Elasto-mechanical analysis with 'Birch stiffness increase' effect

One can separate the pressure effect into an *elasto-mechanical* part and a *material* part (matrix weakening) addressed later as *'2nd Tg shift effect'*. The elasto-mechanical part is automatically included in the elasticity equations but the material part from matrix weakening has to be introduced. Matrix weakening is effective on strengths, elastic constants, ultimate failure strains beyond a distinct hydrostatic pressure and is to be regarded when the experiments are

executed at ambient (room) temperature which is the case in the WWFE-II. The term 2^{nd}Tg shift means that the lower (2^{nd}) glass temperature of a polymer comes to lie above 0° C if the multi-axial pressure exceeds this distinct value. The effect of pressure with respect to a 'healing' of the 'diffuse' micro-cracking is included in the lamina or laminate high pressure test data and cannot be separated as the author believes. In this context it is to be recalled: The pressure-based lowering of the equivalent stress should not be mixed up with an increase of the strength (mind $\sigma_{eq}(\{\sigma\})/\overline{R}=1$).

Investigating the elasto-mechanical part is to consider the pressure-dependent stiffness increase of the polymer solid termed here the *'Birch stiffness increase'* (*finite strain theory*, [25], compressive bulk modulus). This is considered in an additional stiffness correction directly in the usual elasto-mechanical analysis (*infinite strain theory*). Its increase in matrix stiffness is introduced via the cited micro-mechanical equations.

Some insight – in the frame of the elasto-mechanical analysis - can be gained from inserting p_{hyd} into the isotropic Hookean law shown as general formulation (x,y,z system) or as the equivalent formulation in principal stresses (I, II, III system)

$$\begin{Bmatrix}\varepsilon_x\\ \varepsilon_y\\ \varepsilon_z\\ \gamma_{yz}\\ \gamma_{xz}\\ \gamma_{xy}\end{Bmatrix}=\begin{bmatrix}\frac{1}{E} & \frac{-\nu}{E} & \frac{-\nu}{E} & 0 & 0 & 0\\ \frac{-\nu}{E} & \frac{1}{E} & \frac{-\nu}{E} & 0 & 0 & 0\\ \frac{-\nu}{E} & \frac{-\nu}{E} & \frac{1}{E} & 0 & 0 & 0\\ & & & \frac{1}{G} & 0 & 0\\ & (symm.) & & & \frac{1}{G} & 0\\ & & & & & \frac{1}{G}\end{bmatrix}\cdot\begin{Bmatrix}\sigma_x\\ \sigma_y\\ \sigma_z\\ \tau_{yz}\\ \tau_{xz}\\ \tau_{xy}\end{Bmatrix},\quad \begin{Bmatrix}\varepsilon_I\\ \varepsilon_{II}\\ \varepsilon_{III}\end{Bmatrix}=\begin{bmatrix}\frac{1}{E} & \frac{-\nu}{E} & \frac{-\nu}{E}\\ \frac{-\nu}{E} & \frac{1}{E} & \frac{-\nu}{E}\\ \frac{-\nu}{E} & \frac{-\nu}{E} & \frac{1}{E}\end{bmatrix}\cdot\begin{Bmatrix}\sigma_I\\ \sigma_{II}\\ \sigma_{III}\end{Bmatrix},\quad (20)$$

from which follows $E\cdot(\varepsilon_x+\varepsilon_y+\varepsilon_z)=-3\cdot p_{hyd}\cdot(1-2\cdot\nu)$ or $E\cdot\Delta V/V=p_{hyd}\cdot(3-6\cdot\nu)$.

When the material condenses and the volume change ΔV approximates zero this will have an effect on ν the size of which depends on the applied material. For the epoxy matrix it can be assumed that the matrix material becomes denser or that the little pores are reduced and flaws are compressed. The share of the matrix as the only 'yielding' constituent of the UD wrt micro-damage quasi-yielding is not fully clear. At least it depends on the ductility of the chosen matrix material (resin system). In contrast to a yielding metal the inelasticity also depends on some visco-elasticity from the constituent matrix and on micro-mechanical damage. In this paper, the pressure-dependent increase of Poisson's ratio ν is applied as not to change with pressure according to missing information on the relationship to increasing inelasticity. How far Poisson's ratio ν might change wrt the material's compressibility is not provided. However, the sensitivity of a result to ν is sometimes considered by a parameter study.

The hydrostatic pressure-dependent increase of the moduli, measured in experiments, seems to be mainly caused by the finite strains of the polymer. Therefore, Birch [13] utilized the finite strains in his approach, where he still assumed a constant ν. He proposed for the matrix (suffix m deleted here) as 'Birch finite strain modulus increase effect' (Birch effect) for Young's modulus and shear modulus the growth equations

$$E_{hyd} / E_0 = 1 + (-\sigma_{hyd} / E_0) \cdot (10 - 8\nu) \cdot (1 - \nu), \tag{21a}$$

$$G_{hyd} / G_0 = 1 + (-\sigma_{hyd} / G_0) \cdot (9 - 12\nu) \cdot (2 + 2\nu). \tag{21b}$$

In this case, $G \neq E/(2+2\nu)$.

In addition, for the stress analysis some insight on the infinitesimal (squares and products of the strains are neglected) elasto-mechanically-caused pseudo-stiffness change of an isotropic polymer material such as the matrix is obtained by studying a simple elastic model. Essential

for the evaluation is the differentiation of the hydrostatic pressure stress and an additional stress which may act together at the x-cross section. Of course, the associated moduli given above have to be inserted as *E* and *G*. To illustrate this pseudo-stiffness change, elastic behaviour as well as $\nu < 0.5$ is assumed for the model. In this context and in supporting the test data evaluation in WWFE-II, Part B, the following text parts a), b), and c) are performed:

- a) Pseudo-Youngs modulus E^{ps} of an isotropic material:

In case of a monotonically increasing stress state $\{\sigma\}=(\sigma_x^{add}+\sigma_{hyd},\sigma_{hyd},\sigma_{hyd},0,0,0)^T$, which is a simultaneous superposition of a uni-axial additional stress and a hydrostatic stress state, the stress-strain equation

$$E\cdot(\varepsilon_I^{add}+\varepsilon_{Ihyd})=\sigma_x^{add}+\sigma_{hyd}\cdot(1-2\nu)=E\cdot\varepsilon_x^{ps} \qquad (22a)$$

is obtained with the strain ε_x^{ps}, measured under combined loading. For the simple uni-axial loading alone the equation reads

$$E\cdot\varepsilon_x^{add}=\sigma_x^{add}. \qquad (22b)$$

If the normal stress is the same in both cases then $\sigma_x^{add}=E\cdot\varepsilon_x^{add}=E^{ps}\cdot\varepsilon_x^{ps}$ is valid and the ratio of the two strains delivers a function for the change of the Young's modulus

$$\frac{\varepsilon_x^{add}}{\varepsilon_x^{ps}}=\frac{E^{ps}}{E}=\frac{\sigma_x^{add}}{\sigma_x^{add}+\sigma_{hyd}\cdot(1-2\nu)}=\frac{1}{1+f_{hyd}\cdot(1-2\nu)} \qquad (22c)$$

when utilizing the relation $\sigma_{hyd}=f_{hyd}\cdot\sigma_x^{add}$. From this it is obvious (proportional loading) that for tensile stress σ_x^{add} with a $\sigma_{hyd}=-p_{hyd}$ the factor f_{hyd} becomes negative. This means with respect to $E\cdot\varepsilon_x^{add}$ that the slope increases with increasing p_{hyd} or in other words, a pseudo-stiffness increase is elasto-mechanically achieved under hydrostatic compression. For

compressive stress $\sigma_x^{add} = -200MPa$ with $\sigma_{hyd} = -600MPa$ follows $f_{hyd} = +3$, and when setting $\nu = 0.4$, an elasto-mechanically-caused stiffness decrease of 29%. With increasing ν the size of the effect is vanishing according to $(1-2\nu) \to 0$.

-b) Pseudo shear modulus G^{ps} of an isotropic material:

In the case of σ_{hyd} with an additional shear loading τ the shear stress τ can be replaced by two normal principal stresses $\sigma_I^{add} = +|\tau|$ and $\sigma_{II}^{add} = -|\tau|$. This results via the principal load stress vector $\{\sigma\}=(\sigma_I^{add} + \sigma_{hyd}, \sigma_{II}^{add} + \sigma_{hyd}, \sigma_{hyd})^T$ in the equation

$$E \cdot (\varepsilon_I^{add} + \varepsilon_{Ihyd}) = \sigma_I^{add} - \nu \cdot \sigma_{II}^{add} + \sigma_{hyd} \cdot (1-2\nu) = |\tau| \cdot (1+\nu) + \sigma_{hyd} \cdot (1-2\nu). \quad (23a)$$

For the simple uni-axial loading alone the equation reads

$$E \cdot \varepsilon_I^{add} = \sigma_I^{add} - \nu \cdot \sigma_I^{add} = |\tau| \cdot (1+\nu). \quad (23b)$$

If the shear stress is the same in both cases then $|\tau| = \gamma \cdot G = \gamma^{ps} \cdot G^{ps}$ is valid and the ratio of the two shear strains delivers a function for the change of the shear modulus which is proportional to E, according to $\sigma_{hyd} = f_{hyd} \cdot |\tau|$ or $f_{hyd} = -p_{hyd} / |\tau|$

$$\frac{\varepsilon_x^{add}}{\varepsilon_x^{ps}} = \frac{E^{ps}}{E} = \frac{|\tau| \cdot (1+\nu)}{|\tau| \cdot (1+\nu) + \sigma_{hyd} \cdot (1-2\nu)} = \frac{1}{1 + f_{hyd} \cdot (1-2\nu)/(1+\nu)} \quad . \quad (23c)$$

The shear stress increases with p_{hyd} and with increasing ν the size of the effect is vanishing.

c) Pseudo Young's modulus $E_\perp$ of a UD material:

Finally the elasto-mechanically stiffening effect of hydrostatic pressure shall be shortly described for the envisaged UD material. Here, the vector of all the acting stresses $\{\sigma\}_{lamina} = (\sigma_{hyd}, \sigma_2^{add} + \sigma_{hyd}, \sigma_{hyd}, 0, 0, 0)^T$ is to be inserted into the Equation (20b)

$$\begin{Bmatrix}\varepsilon_1\\ \varepsilon_2\\ \varepsilon_3\end{Bmatrix} = \begin{bmatrix}\frac{1}{E_{||}} & \frac{-\nu_{||\perp}}{E_\perp} & \frac{-\nu_{||\perp}}{E_\perp}\\ \frac{-\nu_{\perp||}}{E_{||}} & \frac{1}{E_\perp} & \frac{-\nu_{\perp\perp}}{E_\perp}\\ \frac{-\nu_{\perp||}}{E_{||}} & \frac{-\nu_{\perp\perp}}{E_\perp} & \frac{1}{E_\perp}\end{bmatrix} \cdot \begin{Bmatrix}\sigma_1\\ \sigma_2\\ \sigma_3\end{Bmatrix}. \qquad (20b)$$

Corresponding to the isotropic equation the equation

$$E_\perp \cdot (\varepsilon_2^{add} + \varepsilon_2^{hyd}) = \sigma_2^{add} + \sigma_{hyd} \cdot (1 - \nu_{||\perp} - \nu_{\perp\perp}) \qquad (24a)$$

is obtained and for simple transversal stressing

$$E_\perp \cdot \varepsilon_2^{add} = \sigma_2^{add}. \qquad (24b)$$

with the in-plane Poisson's ratio $\nu_{||\perp}$, and $\nu_{\perp\perp}$ as the transverse one. Again assuming the stress, to be the same in the two cases, delivers the equation $\sigma_2^{add} = \varepsilon_2^{add} \cdot E_\perp = \varepsilon_2^{ps} \cdot E_\perp^{ps}$

from which a relationship, similar to Equation (22c), follows

$$\frac{E_\perp^{ps}}{E_\perp} = \frac{1}{(1 + f_{hyd} \cdot (1 - \nu_{\|\perp} - \nu_{\perp\perp}))}. \qquad (24c)$$

For $f_{hyd} = -p_{hyd} / \sigma_2^{add}$, Equation (24c) results in case of a tensile transversal stress in a stiffness increase.

2.3.2. 2nd Tg shift effect

According to Refs[14,145], nonlinear behaviour of polymers is affected by the presence of high hydrostatic pressure. This special behaviour of the matrix beyond a certain 'knee' point, **Fig. 3a,** is generated because the molecular motion between the cross-links is not frozen anymore. The reason for the occurrence of this knee or kink is attributed to the shift of the second glass transition temperature point, 2ndTg, up to ambient temperature where the tests are performed.

Also the elastic moduli of the UD material become a function of the applied multi-axial pressure.

Considering a UD material, increasing matrix stiffness E_m or G_m increases the resistance of local filament buckling and kinking under compressive loadings. Thus, the stiffness loss of the matrix also affects the strength of the UD material due to a lower stiffening of the embedded filaments.

For taking into account the effect of pressure on the lamina properties, it is important to show first the effect on the matrix properties. Several cases may be encountered:

- *Effect on matrix moduli* E_m, G_m*:*

For an epoxy material, Fig. 3 depicts a bi-linear curve with a knee or inflection point or kink at *200 MPa*, according to [14]. This knee value is typical for the matrix utilized.

From the various cited references a coarse approach can be only constructed on basis of the gathered test results which seem to be relatively generally valid for the epoxy matrix family. The kinked curve can be fitted in the usual high pressure domain in a bi-linear manner by the function (series spring model again)

$$\left(\frac{1}{G_m / G_{m0}}\right)^M = \left(\frac{1}{1 + a_1 \cdot \sigma_{ef}}\right)^M + \left(\frac{1}{a_2 + a_3 \cdot \sigma_{ef}}\right)^M \qquad (25)$$

where a_1, a_2, a_3 are fitting parameters and the M is a weakening exponent. The effect on the shear modulus can be tackled by the basic value G_{m0} at room conditions times (effective beyond the knee point) a reduction factor f_{2ndTg}, termed 2ndTg-shift factor (see **Fig. 3b**)

$$G_m = G_{m0} \cdot f(2ndTg) \quad \text{with} \quad f_{2ndTg} = 1/\sqrt[M]{1 + \left(\frac{1 + a_1 \cdot \sigma_{ef}}{a_2 + a_3 \cdot \sigma_{ef}}\right)^M} \quad . \qquad (26)$$

To be inserted into this equation is an effective hydrostatic stress value

$$\sigma_{ef} = (\sigma_{I,m} + \sigma_{II,m} + \sigma_{III,m})/3 \quad \text{with e.g.} \quad \sigma_{I,m} = \varepsilon_1 \cdot E_{\parallel} \cdot V_f{}^2/(1-V_f) \qquad (27)$$

wherein the σ_l are the smeared principle stresses of the matrix at the envisaged critical location within the embedded constrained lamina. Both quantities, σ_{ef} and σ_l are sign-dependent. This means the pressure is inserted as a negative value and a hydrostatic tensile stress as a positive value. Equation (27) involves the possible hydrostatic stress σ_{hyd} and external stresses $(\sigma_1, \sigma_2, \sigma_3)$ applied to the matrix. Note: The term σ_{ef} is nothing else but the factorized first invariant of the stress tensor.

The decrease of the E- or G-modulus is similar according to Fig3a, for PR319 epoxy material. The effect is considered by the 2nd shift correction factor f_{2ndTg}, depicted in Fig.3b which is taken as typical curve, due to a lack of information in the input data of WWFE-II.

- *Effect on matrix strengths:*

For the matrix strength, Pae showed in [14] that the effect on strength loss is higher than that for the moduli. As information was provided in WWFE-II, the factor f_{2ndTg} is fully applied in the test cases if not indicated otherwise.

- *Transfer to UD stiffnesses and strengths:*

The physical behaviour of the matrix has to be considered when predicting a matrix-dominated UD material behaviour. For the UD material, the 2ndTg-effect and therefore the reduction will differ from that which was obtained for the matrix, the effect is usually minor. However, lacking of a provided input for the materials, in the Test Cases the strength reduction according to Equation (26) will be simply transferred from the matrix to the UD

material strengths. In cases where more knowledge seems to be available the reduction is indicated.

2.3.3. In-situ effect or constraint effect of embedded laminae

In-situ strengths of a lamina which is here a layer of a laminate depend on its thickness (for this so-called 'thin-layer effect') and on the location in the laminate, that means whether the layer is fully embedded or just an outer layer that is more jeopardized by fracture mechanics-based micro-cracking generating a decrease of the effective moduli.

For the description of the full non-linear stress-strain curve (**Fig. 4**), this includes (strain-) hardening and (strain-)softening of the embedded lamina, it is important that the peak value of the effective stress-strain curve is higher than the strength point $\overline{R}$ of the isolated specimen due to the change from the 'weakest link' behaviour to a redundant behaviour. In the IFF conditions the classical strength values should be replaced by their respective in-situ values. See e.g. [28], in which fracture-mechanical, strain-energy-based strengths $\overline{R}_{\perp||}^{in-situ}$, $\overline{R}_{\perp}^{t,in-situ}$ were developed. For reasons of numerical simplicity this peak effect is flattened in the proposed approach for mapping the softening branch. For the execution of nonlinear analysis the application of such an *effective* stress-strain curve is very practical. It approaches the behaviour of the lamina in the laminate regarding the stack, its position, and the thickness. It is to be noted that after the onset of IFF only 'smeared' stresses can be calculated for the micro-cracked lamina and are inserted into the failure conditions. These stresses are smeared over some length of the cracking lamina, a length which includes a number of micro-cracks. Therefore, the in-situ effect will be covered by the choice of the softening curve.

2.4. Description of non-linearity

2.4.1. General

Four sources of non-linearity will be considered in the analysis:

- non-linear stress-strain behaviour of the smeared lamina material (hardening, below IFF),
- the degradation-related softening above the IFF level,
- non-linear behaviour including large strains and large deformations if applicable, and
- non-linearity from weakening of the pressure level-dependent matrix behaviour.

These are described below.

2.4.2. Mapping of hardening and softening (degradation curve)

For the envisaged strain-hardening FRP materials the Ramberg-Osgood equation

$$\varepsilon = \sigma / E_0^{mode} + 0.002(\sigma / \overline{R}_{p0.2}^{mode})^n \qquad (28a)$$

$$\gamma_{21} = \tau_{21} / G_{||\perp} + 0.002\cdot(\tau_{21} / \overline{R}_{p0.2\perp||})^n . \qquad (28b)$$

can be used as mapping (fitting) approach, The Ramberg/Osgood exponent

$$n = \ell n\left(\varepsilon_{pl}(R_m)\right) / \ell n\left(\overline{R}_m^{mode} / \overline{R}_{p0.2}^{mode}\right) \qquad (29)$$

is estimated from strength point $\left(\overline{R}_m^{mode},\ \varepsilon_{pl}(\overline{R}_m^{mode})\right)$ and yield point information.

For the laminate Test Cases, a softening model is needed beyond initial failure. The approach used is based on the idea that the softening function is factorizing the Ramberg-Osgood hardening function. A simple function was used to map this softening in order to later derive the secant modulus for the non-linear analysis. It reads ($\exp[z] = e^z$)

$$\sigma_{soft} = \overline{R}_m /(1+exp[(a_{soft} + \varepsilon)/ b_{soft}]) = \overline{R}_m \cdot \eta \qquad (30)$$

Where η is a degradation function. The two curve parameters a_{soft}, b_{soft} are determined from data of two calibration points at least or curve fitting if test data is available in the softening domain,

$(0.995 \cdot \overline{R}_m\,,\ \varepsilon\,(\overline{R}_m))$ and e.g. $(0.1 \cdot \overline{R}_m\,,\ \varepsilon\,(0.1 \cdot \overline{R}_m))$ (31)

(applying point $1.0 \cdot \overline{R}_m\,,\ \varepsilon(\overline{R}_m)$ is numerically not permitted!).

For the non-linear analysis procedure, data for the secant moduli of $E_{\perp}^{c}$ and $G_{||\perp}$ may be derived from the hardening equation, Equation (30), as

$$E_{sec}^{hard} = \frac{\sigma}{\varepsilon} = \frac{\sigma}{\frac{\sigma}{E_0} + 0.002 \cdot (\frac{\sigma}{\overline{R}_{p0.2}})^n} = \frac{E_0}{1 + 0.002 \cdot \frac{E_0}{\overline{R}_{p0.2}} \cdot (\frac{\sigma}{\overline{R}_{p0.2}})^{n-1}} \quad . \tag{32}$$

Hence the equation for the secant modulus given as

$$E_{sec} == \frac{E_0}{1 + 0.002 \cdot \frac{E_0}{R_{p0.2}} \cdot (\frac{\sigma \cdot \eta}{R_{p0.2}})^{n-1}} \quad \text{with} \quad \eta = \frac{1}{1 + exp(\frac{a_{soft} + \varepsilon}{b_{soft}})} \tag{33}$$

describes the full domain by applying the degradation function η. It describes the softening-associated degradation of the UD material. According to the definition of the secant modulus, Equation (32), η (equals 1 in the hardening domain) may be also directly put on E_{sec} in the analysis instead on σ according to their linear relationship.

2.5. Post-initial failure modelling (softening branch curve)

Degradation beyond IFF, in the post-initial failure regime, is termed here softening. Softening is treated differently. The FMC uses an assumed softening function (evolution equation) for all three IFF curves.

2.6. Residual stresses and curing stresses

2.6.1 General on residual stresses

Residual stresses (suffix $_R$) are taken into account by superimposing them onto the external load stresses (suffix $_L$)

$$\{\sigma\} = \{\sigma_L\} + \{\sigma_R\}. \qquad (34)$$

Such residual stresses in the laminae of the laminate decay with decreasing stiffness, caused by the matrix degradation due to micro-cracking, which accompanies increasing non-linearity.

2.6.2 Curing stresses in a matrix

Once the part starts to solidify residual stresses may build up as a result of a constrained straining within the structural part, e.g. an inclusion in the polymer. In a homogeneous thick epoxy polymer matrix specimen the curing stress is very low, around 1 MPa is cited in [16].

2.6.3 Curing stresses between filament and matrix and in the laminae

Chemical cross-linking leads to a volume shrinkage during the liquid-solid transition or in the so-called glass transition domain, respectively. The cure-induced residual stresses are generated after the polymer reaches the gel point during curing. Contractions in the solid phase contribute to residual (built-in) stresses, see [17]. Thereby, this chemical shrinking causes physical shrinking and residual (normal) stresses when a lamina or – the more – a laminate is cooled down from its stress-free temperature to room temperature.

Including fibres into the polymer matrix produces filament stresses due to curing shrinkage and according to different CTEs of the constituents, the solidifying matrix and the filament. Between the filament and the filament-embedding matrix the matrix shrinks and produces residual compressive stresses normal to the filament. Shrinkage of resin pockets causes tensile stresses [18,19].

There are curing stresses of the 1st kind (lamina material level, as part of laminate; *macro*mechanical curing stresses) and of the 2nd kind (fibre-matrix level; *micro*mechanical curing stresses]). The latter are assumed to be included in the strength values. Hence forth, residual stresses of the 1st kind will be only considered.

2.6.4 Conclusions for a multi-ply laminate

As temperature drop the difference *stress-free* temperature minus *room* temperature as *effective* temperature difference is applied in order to consider the effect of the residual stresses of the 1st kind. Moisture may be assumed here to have a balancing effect of 30°C.

2.7. Effects in thick composites

Owing to refined curing procedures, curing of thick parts without obtaining too high curing stresses became possible. In general however remains, curing of a thick wall normally ends up with higher curing stresses than in the case of thin walls. In [20] was shown that the difference between surface curing stress (exterior, tensile) and interior curing stress (interior, compressive) was becoming of interest when the thickness was higher than 5 mm. In this not yet engineering application the difference was just about 4 MPa.

2.8. Variation of moduli $E_{\perp}, G_{\parallel\perp}$ and Poisson's ratio $\nu_{\perp\parallel}$

The elaborations in [21] indicate for CFRP that the IFF1 microcrack-related loss of $E_{\perp}$ is significant but that the IFF3 degradation causes just a marginal loss of $G_{\parallel\perp}$. Further, the influence of damage on the larger Poisson's ratio was also marginal. For the differently critical wedge failure IFF2 data was not delivered.

The alteration of the major Poisson's ratio (here termed $\nu_{\perp\parallel}$) is linked to successive micro-cracking which the generation of micro-spaces. Hydrostatic compression impedes the generation of micro-spaces. Possessing no input for Poisson's ratio and with respect to the quality of the other affecting properties, the value is kept constant in the analyses.

With increasing micro-damage state the UD composite may become orthotropic and the Poisson's ratios should be treated differently, $\nu_{31} \neq \nu_{21}$.

3. Description of data input and Test Cases in the WWFE-II

Details of 12 Test Cases (TC) are provided in Ref[7]. These include:

-Material properties of the UD lamina and its constituents

-Two important and widely used classes of fibres (carbon and glass)

-Five types of fibres; two types of glass fibres and three types of carbon fibres, giving the following UD laminae:

1.) E-Glass/MY750, 2.) S2-Glass/epoxy, 3.) AS carbon/epoxy,

4.) IM7/8551-7 carbon/epoxy, and 5.) T300/PR319 carbon/epoxy.

-3D elastic constants, thermal properties, failure strains and strengths and nonlinear stress-strain curves for the five UD laminae. The UD lamina material is treated as a transversely-isotropic continuum (confirmed by the provided input properties):

$$E_2 = E_3 \ , \ G_{12} = G_{13} \ , \ \nu_{12} = \nu_{13} \ , \text{ and } \ G_{23} = E_2 /(2 + 2 \cdot \nu_{23}) . \tag{35}$$

Five types of laminates were chosen for the analysis

(1) Pure resin matrix (TC1),

(2) 0° UD lamina (TC2-TC7),

(3) Angle ply $[35/-35/35/-35]_s$ laminate (TC8, TC9),

(4) Quasi-isotropic $[45/-45/90/0]_s$ laminate (TC10),

(5) Cross-ply $[0/90/0/90]_s$ laminate (TC11, TC12).

4. Comments on the input for the analysis

4.1. Comments on the provided properties and test cases

Unfortunately for PR319 epoxy, where the matrix information is needed for tackling the TC 2 through TC 4 tasks, accurate basic values are missing. The provided Young's moduli do not match well with the given stress-strain curves. Some curves are shorter than the table value indicates.

-Information on the effect, which the author termed the 2ndTg shift, was not provided.

-No micro-mechanical formulas were provided and therefore the author relied on those reported in [9].

-No information was provided to assess the values of the *physically* required friction parameters $b_{\perp}^{c}$, $b_{\perp\parallel}$ and therefore they were assumed according to the author's experience.

4.2. Assumptions for the predictions

All 'full failure theory models' require the knowledge of quite a large number of parameters. This includes in the case of the FMC-based UD failure theory (for other theories similar) parameters for the three parts of a failure theory the requirement of:

a) Macro-scopic failure conditions of the transversely-isotropic UD material: 5 strengths data from 'isolated' tests + 2 friction parameters +1 mode interaction exponent m + fibre and matrix data (if the pressure dependent stiffness and strength properties are not given as lamina information but as matrix information.

b) Stress-strain analysis: 5 elastic constants, 2 coefficients of thermal expansions, 2 coefficients of moisture expansion, 1 stress free temperature.

Non-linear analysis for each mode: 1 strain to failure, 2 hardening parameters (Ramberg-Osgood exponent + 'yield' strength $\overline{R}_{0.2}$) and 1 point for the determination of the softening parameter (the 2nd one is fixed by the strength point $\overline{R}$), and the slope constant $c_{\gamma Pae}$ (TC 3). The $2^{nd}Tg$ curve fitting parameters (M, a, b c).

In the context above the assumptions made are listed in the following:

* Hydrostatic pressure acts on all cross sections or front faces of the test specimen, an applied external mechanical stress acts on top of one or two cross sections (due to assumed test rig).

* The first FF1 or FF2 is final failure. Also IFF2 (wedge failure) may cause final failure through delamination.

* The void content is negligible (< 1%). Otherwise, the IFF2 approach would have to be modified by an invariant representing a volume change to consider the porosity (see [3]).

* The parameters $m = 2.8;\ b_{\perp}^{c} = 1.21\ (\Theta_{fp}^{c}\,° = 50°),\ b_{\perp||} = 0.3$ were estimated and are basis set for all laminae.

* If applicable, residual stresses from the curing cycle are to be computed for the difference 'stress free temperature to room temperature 22°C' as an effective temperature difference.

* The stress-strain curves are average curves, which is the type one needs for test data mapping. Considering curing or moisture stresses (here, the specimens are assumed to be well conditioned) the graphs do not begin in the origin.

* Edge effects are neglected.

* The progressive behaviour of $E_{||}^{t}$ (up to 10%) in the case of C-fibre rovings is not regarded.

* The course of each softening curve is assumed. Post-initial IFF is considered by gradually degrading properties of the embedded lamina.

* The Ramberg/Osgood exponent *n* was computed/estimated from the provided curve data. The softening parameters a_{soft} ,b_{soft} are determined from the assumed softening curve with one point of it at a strain about two times the 'isolated lamina failure strain'.

* The $2^{nd}Tg$ shift effect - as a matrix attribute - is mainly affecting the matrix-dominated behaviour of a lamina which means compressive and shear behaviour. In these cases the associated reduction factor f_{2ndTg}, derived from the matrix behaviour, is applied to the UD material, too, due to missing knowledge but it is scaled for the specific Test Case.

* The hydrostatic pressure effects is considered by applying the *'Birch stiffness increase'* equations Equation (21) together with the corresponding micromechanical formula.

5. Theoretical predictions

For eleven Test Cases the analyses were performed using a MathCad computer code. TC 10 was not analysed, due to a lack of time. A simple self-correcting secant modulus approach is utilized in the nonlinear analysis. The solution procedure of the nonlinear analysis is to establish static equilibrium at each load step after material properties have been changed. For each iteration the procedure is repeated until convergence (equilibrium). By employing the equivalent stress, the associated secant modulus of each IFF mode $E_{sec}(\sigma_{eq}^{mode})$ is determined for the hardening and the softening regime. For additional details see Annex 2

5.1 Test case 1, Matrix MY 750, $\{\sigma\} = (\sigma_x,\ \sigma_y = \sigma_z,\ \sigma_z,\ 0,\ 0,\ 0)^T \equiv (\sigma_I, \sigma_{II}, \sigma_{III})^T$

The 'isotropic' FMC-based failure conditions for the occurring normal fracture (NF) and for shear fracture (SF) are, [22,23]

$$\text{NF: } 0.5\frac{I_1 + \sqrt{4J_2 - I_1^{\,2}/3}}{\bar{R}_t} = 1 \quad \text{and} \quad \text{SF: } a_\tau^c \cdot \frac{6J_2 \cdot \Phi}{\bar{R}_c^{\,2}} + b_\tau^c \cdot \frac{I_1}{\bar{R}_c} = 1 \qquad (36a, b)$$

The parameter Φ represents the so-called 120°-symmetry of brittle isotropic materials. Due to the fact that MY750 is not so brittle Φ can be set one. Following the work in [24,4,22] a volume change is linked to the square of the first invariant I_1 (Equation (30) of the stress tensor whereas Huber-Mises-Hencky's (HMH) 'shear yielding'-describing invariant J_2, ($\sigma_{eq}^{Mises} = \sqrt{3 \cdot J_2}$), is linked to the deviator with $\sigma_I, \sigma_{II}, \sigma_{III}$ as principal (normal) stresses:

$$I_1 = \sigma_I + \sigma_{II} + \sigma_{III}\,, \qquad (37)$$

$$J_2 = [(\sigma_1 - \sigma_{II})^2 + (\sigma_{II} - \sigma_{III})^2 + (\sigma_{III} - \sigma_I)^2]/6 = 4 \cdot (\tau_{III}^2 + \tau_{II}^2 + \tau_I^2) = f(\tau).$$

The J_2 formulation is given above in principal shear stresses, too.

If there would be a change in the volumetric strain ('no constant volume process') this is to be captured by the failure condition. Then, $I_1^{\,2}$ must enter the failure condition of the matrix. This term represents a volume change due to Beltrami, [24]). Because it may be assumed for the actual matrix that practically no voids or resin pockets are in the matrix specimen (means 'dense' consistency or non-porous material) then an additional part I_1^2 is not to include into the Equations (36 a and b) to describe this feature. In a porous material situation the SF mode is replaced by a so-called crushing mode.

In order to determine the two curve parameters in Equation (36), the following steps are taken. Inserting the compressive strength $\sigma_1 = -\overline{R}_c$ into Equation (36b) delivers

$$a_\tau^c \cdot \frac{2\overline{R}_c^{\,2}}{\overline{R}_c^{\,2}} + b_\tau^c \cdot \frac{-\overline{R}_c}{\overline{R}_c} = 1 \ , \qquad (38a)$$

And this gives the following:

$$2a_\tau^c = (1 + b_\tau^c). \qquad (38b)$$

It remains the estimation of the still unknown 'friction parameter' b_τ^c. Its value is related to Mohr's fracture angle which is to be measured in tests. Considering the information above, the value for the fracture angle of this semi-brittle MY750 should not be much higher than the zero friction angle value, which is 45° for ductile behaviour. From this follows, a fracture angle of Θ_{fp}^c = 47° can be assumed. When determining the friction parameter from the fracture angle, then Equation (36b) has to be transformed into a Mohr-Coulomb formulation. This procedure results in the formula

$$b_\tau^c = (-3 \cdot C_{fp}^c + 1)/(3 \cdot C_{fp}^c + 1) \quad \text{with} \quad C_{fp}^c = cos(2 \cdot \Theta_{fp}^c{}^\circ \cdot \pi / 180^\circ) \; . \tag{39}$$

Hence, for $\Theta_{fp}^c{}^\circ = 47^\circ$ a parameter value $b_\tau^c = 1.53$ is computed and applied for all test cases.

Thus, the effort equations read:

$$Eff^{\sigma} = 0.5 \frac{I_1 + \sqrt{4J_2 - I_1{}^2/3}}{\overline{R}_t}, \tag{40a}$$

$$Eff^{\tau} = \frac{b_\tau^c \cdot I_1 + \sqrt{(b_\tau^c \cdot I_1)^2 + 24 \cdot a_\tau^c \cdot J_2}}{2 \cdot \overline{R}_c} \; , \quad a_\tau^c = 0.5 \cdot (1 + b_\tau^c) \tag{40b}$$

with the invariants I_1, J_2 from Equation (37) which – as mentioned - should not be mixed up with the UD invariants in Equation (3). The superscripts $^{\sigma}$ and $^{\tau}$ mark the fracture governing stress in the physical fracture plane (Mohr).

It has to be checked now "How the matrix material is behaving, brittle or ductile or mixed?". Due to material symmetry, isotropic brittle and semi-brittle behaving materials possess just two strengths. The additionally provided 'shear strength' (sometimes termed as cohesive strength R_τ) is therefore a fully dependent value and its coordinates should fully lie on the NF failure curve if the material behaves fully brittle. However, this is not true as Figure 5 indicates. R_τ is neither located on the NF nor on the SF curve. So it may be assumed from the provided strength values: This matrix material is semi-brittle. This is proven by the relatively small difference between tensile strength and compressive strength. And it can be further substantiated by inserting a stress $max\tau$ into the Equation (40). With the invariants $I_1 = 0$ and $J_2 = max\tau^2$ Equation (40b) predicts $max\tau_{SF} = 44 \; MPa$ for $b_\tau^c = 1.53$. Inserting the invariants above into the NF condition, Equation (40a), yields $max\tau_{NF} = \overline{R}^t = 80 \; MPa$. Therefore, the provided $\overline{R}_\tau = 54 \; MPa$, is a fracture value of an interaction zone of two modes

NF and SF. From that it can be also concluded that the MY750 matrix is semi-brittle. This also proves $\Phi \cong 1$ in Equation (36b).

To be noted: The stiffness increase upon p_{hyd} was applied according to Birch's formula. An interaction of the two failure mode curves F^{σ} (NF) and F^{τ} (SF) made problems due to the above proven fact that the MY750 matrix is semi-brittle. Then the application of the simple interaction equation Equation (16) can not handle this, see Figure 5a,b. Therefore, as engineering approach, a simple linear interaction line in the 3D domain (Figure 1a) delivered the requested interaction curve. Also to be assumed is a confining cap. The Figure 5a,b outline the final failure curves in the 3D domain. Figure 1b depicts the situation in the 2D domain.

Essential results:

* As the matrix material is semi-brittle a fracture failure surface or a failure envelope (curve) can be determined which confines the consecutively growing yield surface. However, this growing yield surface is not shown in Figure 5c,d. Basically, in the positive quadrant NF will occur and in the negative quadrant SF failure (denoted by F^{σ} and F^{τ}), Figure 5c,d.

* The matrix is assumed to be dense (no voids) and therefore can be infinitely compressed when subjected to tri-axial compression (solid line). The consideration of matrix softening above the 'knee' at about $200\ MPa$ has a substantial influence in the high pressure regime (dashed line). Shear fracture is activated if the difference of the stresses in a section plane is large enough to cause fracture according to IFF2. This is possible for two stress combinations associated to the two failure curves.

* For giving a global understanding on a multi-fold failure the NF mode-related multi-axial strengths $\overline{R}_{tt}, \overline{R}_{ttt}$ were estimated and depicted in Figure 1d.

* Stiffness and strength of the polymer, $max\sigma_x$ decreases with p_{hyd} beyond 200 MPa. The $2^{nd}Tg$ shift effect causes an earlier fracture.

* Viewing Figure 1 a, it can be simply drawn from the NF curve that $\overline{R}_\tau \neq \tau_{fr}^{NF} = \overline{R}_t$ because it does not lie on the respective point (cross x) of the abscissa which is computed from the NF equation via $I_1 = 0,\ \sqrt{J_2} = \overline{R}_\tau$ as $\sqrt{2 \cdot J_2} / \overline{R}_c = \sqrt{2} \cdot 80 / 120 = 0.94$. From literature as a thumb rule may be applied: Brittle behaviour is usually dedicated to an aspect ratio $\overline{R}_c / \overline{R}_t > 3$. This is much higher than 0.94. Again it is proven: The matrix is semi-brittle.

5.2. Test Case 2, UD lamina T300/PR319, $\{\sigma\} = (\sigma_1,\ \sigma_2,\ \sigma_3\ 0,\ 0,\ \tau_{21})^T$

.

The fracture failure curve $\tau_{21}(p_{hyd})$ with $\sigma_1 = \sigma_2 = \sigma_3 = -p_{hyd}$, and p_{hyd} an absolute pressure value is shown in Figure 6.

The shear strength will increase due to the pressure-improved adhesion of the filament-matrix interface with the suppression of the flaw effects [25]. With the increase of p_{hyd} the shear modulus and shear strength as well will increase. For the matrix-dominated shear strength a reduction function f_{2ndTG}, derived for the MY750 matrix, serves as a standard reduction function and is also fully applied in TC1.

Essential results:

* The result of TC 2 is a combined multi-axial *failure state of stress* which may be termed *multi-axial strength*. The elasto-mechanical effect of p_{hyd} is displayed in Figure 6 by the solid curve. It shows that the fracture shear stress changes approximately linearly with p_{hyd} starting from atmospheric pressure level. The reduction in strength (strength weakening effect) of the

matrix material above the knee is indicated by the dashed curve. Due to the bi-linear simple engineering fitting approach the numerical effect still begins at zero.

* There is one driving failure mode, shear failure IFF3. In the high hydrostatic compression domain the failure curve becomes closed by FF2, see Figure 6b.

* The sensitivity to the unknown friction parameter $b_{\perp\|}$ is studied by the choice of two values (0.3, 0.4) for the basic curve (for these two curves is set $f_{2ndTG} = 1$). The result is: the higher the friction, the higher the fracture shear stress.

> *Mind*: The strength of a UD lamina, be it isolated or embedded, practically is not expected to exceed the longitudinal compressive strength ($\overline{R}_{\|}^{c}$) of the lamina. This is clear from Equation (18b) where the left hand side should not exceed 1. However, the results in Fig TC 2b (and later TC 5, 6, and 8) seem to show that the UD strength under bi-axial, tri-axial pressure exceeds the UD longitudinal strength by a large margin. This comes from the elasto-mechanical effect "Poisson's ratio reduces the filament compressive stress $\sigma_{\|f}^{c}$". Explanation for this is: Not the macro-strength but the strain-dominated filament strength is fracture responsible. In other words, the effective compressive stress is decreased, and this effect is automatically considered in the analysis. Further it is to be kept in mind in general: not a single stress within a stress state is fracture responsible but a mode-related equivalent stress, Equation (14), $\sigma_{eq} < \overline{R}$.

5.3. Test Case 3, UD lamina T300/PR319, $\{\sigma\} = (-p_{hyd},\ \sigma_2 = -p_{hyd},\ -p_{hyd},\ 0,\ 0,\ \tau_{21})^T$

The effects of the hydrostatic pressure p_{hyd} on the in-plane fracture shear strain is shown in Figure 7.

Necessary for the establishment of the shear strain failure curve is the relationship of the fracture shear stress τ_{21}^{fr} and p_{hyd}. However, information how the fracture shear stress is

linked to the fracture strain is not known. The increase of $\tau_{21}(p_{hyd})$ and of $G_{12}(p_{hyd})$ is not proportional according to the *2nd Tg shift*. In order to solve this problem, a simple approach was attempted by searching equivalent test results in the literature. From [14] could be concluded that an approximately linear relationship exists between fracture strain and fracture stress, namely

$$\gamma_{21}^{fr} = \gamma_{21}^{fr,initial} + c_{\gamma Pae} \cdot (\tau_{21}^{fr} / \overline{R}_{\perp\parallel} - 1) \qquad (41)$$

with the slope constant $c_{\gamma Pae} = 0.090$. This value has been applied for this Test Case and the following ones. The 2nd Tg considering failure shear strain at $-600 MPa$ is estimated as $\gamma_{21}^{fr,-600} = 15\ \%$.

Essential results:

* The mechanical effect of p_{hyd} leads to an almost linear stress-strain curve (Figure 7).

* The influence of the *2nd Tg shift* effect is demonstrated by the difference of the solid to the dashed curve.

5.4. Test Case 4, UD lamina T300/PR319, $\{\sigma\} = (-p_{hyd},\ \sigma_2 = -p_{hyd},\ -p_{hyd},\ 0,\ 0,\ \tau_{21})^T$

The shear stress strain curves $\tau_{21}(\gamma_{21}^{fr})$ at $p_{hyd} = 600\ MPa$ are shown in Figure 8.

The R-O equation is well mapping the shear stress-shear strain curve at zero pressure. Therefore it is also taken as mapping function for the hydrostatic pressure case with the consequence to determine the associated R-O parameters.

At first a value for the strength $\tau_{21}^{fr,-600}$ at p_{hyd} = *600 MPa* was estimated by the used IFF3 failure condition as *193 MPa,* not respecting the *2nd Tg shift* effect. In [26] a prediction is

given, based on measured shear moduli G_{m0} of the matrix and the micro-mechanical approach which resulted in a high stiffness increase of 79% at $-600MPa$ of the initial shear modulus due to p_{hyd}. Pae and Shi [14,18] reported an increase of 13%. An average value, computed from these two extreme observations, is utilized in the TC 4 analysis: $G_{12}^{-600} = (1.75 + 1.13) \cdot G_{||\perp} \cong 1.4 \cdot G_{||\perp}$ as basis for the R-O parameter determination

$$\gamma_{21}^{-600} = \tau_{21}^{-600} / G_{12}^{-600} + 0.002 \cdot (\tau_{21}^{-600} / \tau_{0.2,21}^{-600})^{n^{-600}} \tag{42}$$

with $$n^{-600} = \ell n\left(\Gamma_{21}^{-600} / 0.002\right) / \ell n\left(\tau_{21}^{fr,-600} / \tau_{0.2,21}^{-600}\right)$$

and $\Gamma_{21}^{-600} = (\gamma_{21}^{fr,-600} - \tau_{21}^{fr,-600} / G_{12}^{-600})$, with $\gamma_{21}^{fr,-600}$ after Equation (41),

as plastic shear strain at *-600 MPa*. Its value can be extracted from TC 3 and counts, if not yet regarding the $2^{nd}Tg$ *shift* effect, $\Gamma_{21}^{-600} = 4.7\ \%$. With the equations and data above one parameter is still unknown, $\tau_{c0.2,21}^{-600}$. According to [18], an estimation is made simulating the shape of his fig. 11. The result was $\tau_{0.2,21}^{-600} = 125\ MPa$.

The 2^{nd} *Tg* curve in Figure 8 is obtained by assuming similarity and a fracture point $(165MPa,\ 15\%)$.

Essential results:

* The effect of p_{hyd} indicates, due to Equation (36), an increase of the initial shear stiffness demonstrated by the deviation of the bold curve from the thin solid line which is the zero pressure curve (Figure 8). The influence of $2^{nd}Tg$ *shift* effect is depicted by the dashed curve.

5.5. Test Case 5, UD lamina E-glass/MY750 Epoxy , $\{\sigma\} = (\sigma_1 = \sigma_3,\ \sigma_2,\ \sigma_3,\ 0,\ 0,\ 0)^T$

The predicted failure envelope is shown in Figure 9 where the stress σ_2 is plotted against σ_1 (= σ_3). In the tension quadrant, uni-axial and bi-axial tensile IFF1 failure will occur, see detail zoom of Figure 9. In the negative quadrant, wedge failure ($F_{\perp}^{\tau}$), IFF2, occurs due to the fact that there is always a difference between σ_3^c and σ_2^c. The initiation of a wedge failure is equal to the onset of delamination damage. The wedge will slide and then locally cause a compressive reaction σ_3^c normal to the lamina's plane onto the adjacent laminae. This will induce delamination or might increase an original delamination. In the case of a tube specimen loaded by a hydrostatic compressive state of stress (no delamination possible), one can conclude also from experience that the multi-axial strength is increased (σ_3^c and σ_2^c are acting in a favourable manner) as long as the sliding friction is increased until a possible maximum. Such a maximum is reached when the combined lateral compressive loading would lead to a FF failure which is here FF2 ($F_{||}^{\tau}$), 'kinking' failure. This situation comes up far beyond *1000 MPa* which means outside the actually practiced engineering domain. Since the Poisson effect reduces the applied fibre-parallel compressive stress, due to the superimposed σ_3^c stress, the tensile failure mode $F_{||}^{\sigma}$ cannot be obtained.

For TC 5 as for the following Test Cases a fracture angle of $\Theta_{fp}^c = 50°$ was assumed. This results in a 'friction parameter of $b_{\perp}^{\tau} = \frac{1}{1+\cos(2\Theta_{fp}^c)} = \frac{1}{1-\mu_{\perp\perp}} = 1.21$. As associated Mohr-Coulomb friction coefficient is computed $\mu_{\perp\perp} = 0.17$. It is a value which is fully related to the chosen linear Mohr-Coulomb approach.

Essential results:

* Two IFF2 fracture situations are depicted by the two sketches in Figure 9. Two curves are resulting from the fact that two differences of the stresses σ_2 and σ_3 may become possible.

* The observation of the FF2 stress effort, $F_{||}^{\tau}$, in the calculation output when uploading, indicates that the two failure curve branches will close at values outside of the so far envisaged domain beyond the 1000 MPa level. Additional coding work on Equation (18b) to derive the closed interaction (each IFF2 with FF2) failure curve was performed in this more academically interesting domain. Figure 9 shows the closed non-failure area. The 'sharp' corner in the negative quadrant is the result of the agreed and chosen deterministic modelling using average input data (survivability, 50% expectation). A probabilistic treatment of the situation in the corner, analogous to Ref.[27], would exhibit that the lines of constant survivability would round the corner (Figure 9) according to increasing survivability values versus the origin of the coordinate system. However this approach would require besides the deterministic mechanical modelling a) a stochastic modelling of the uncertain basic variables (design parameters, especially the *R*), b) the so-called logical modelling of the failure system (for the laminae in a laminate failure system), and c) probabilistic analysis employing e.g. a First-Order-Reliability-Method or a Monte Carlo method in order to grasp the joint-failure probability for a criticality judgement.

*A strong influence of the unknown friction parameter $b_{\perp\perp}$ is indicated (dotted curves) for lower pressures by the variation of its value, semi-brittle (1.21) and brittle (1.52). This highlights the sensitivity to the input data.

* The non-depicted $2^{nd}Tg$ *shift* effect curves would lie marginally outside of the bold curves.

5.6. Test Case 6, UD lamina S-glass/Epoxy, $\{\sigma\} = (\sigma_1,\ \sigma_2,\ \sigma_3 = \sigma_2,\ 0,\ 0,\ 0)^T$

Due to the equal transversal stresses IFF2 cannot occur. However, these two stresses cause filament straining under the activated bi-axial pressure loading wrt to the Poisson effect which leads to two failure curves. The results in Figure 10 show the following:

* The solid curves in the lower part display how much external longitudinal stress (σ_1^t or σ_1^c) can be applied to the material. In the regime $\sigma_2^c = \sigma_3^c > -10R_\perp^c$ no additional external fibre-parallel tensile stress σ_1^t can be carried by the UD material anymore. This proves the limited applicability of the homogenized lamina stresses, because σ_1 is not the fracture stress but $\sigma_{1f} \cong \varepsilon_1 \cdot E_f$. In order to remain on composite level in the third quadrant σ_{1f} has to be multiplied by the fibre volume fraction V_f, as an engineering approach.

* The σ_1 strength decreasing *2^{nd}Tg shift* effect is considered by the dashed line. Its size is not known to the author. However, some reduction (50% of the generally fixed value) is considered and displayed for FF2 which is matrix-dominated. The right curve is not affected.

* The envelope is open in compression-compression quadrant.

5.7. Test Case 7, UD lamina A-S carbon/epoxy1, $\{\sigma\} = (\sigma_1,\ \sigma_2,\ \sigma_3 = \sigma_2,\ 0,\ 0,\ 0)^T$

This is similar to TC 6, except that the UD material is different. The results in Figure 11 show that FF1 is met at a higher bi-axial pressure level $\sigma_2 = \sigma_3$ - in comparison with TC 6, due to the high tensile strength. The predicted envelope is open.

5.8. Test Cases 8, laminate E-glass/MY750 ep., $\{\hat{\sigma}\} = (\hat{\sigma}_x = \sigma_z,\ \hat{\sigma}_y\ , \sigma_z = -p,\ 0,\ 0,\ 0)^T$

Figure 12 depicts the predicted envelope describing the initial and final failure (fracture) stresses. The following observations may be made:

- Quadrant 1: Delamination (IFF1), caused by σ_3^t in $\{\sigma\} = (\approx 0, \sigma_2^t, \sigma_3^t, 0, 0, \tau_{21})^T$

- Quadrant 2: First a benign IFF1, basically caused by σ_2^t in $\{\sigma\} = (\approx 0, \sigma_2^t, \sigma_3^c, 0, 0, \tau_{21})^T$. Then transition and finally interaction of IFF2 and IFF3

- Quadrant 3: Transition from initial failures IFF2/IFF3 to final kinking failure FF2 by altering stress state $\{\sigma\} = (\sigma_1^c, \sigma_2^c, \sigma_3^c, 0, 0, \tau_{21})^T$

- Quadrant 4: Benign IFF2, caused by σ_2^c in $\{\sigma\} = (\sigma_1, \sigma_2^c, \sigma_3^t, 0, 0, \tau_{21})^T$. Then transition and interaction to combined initial failure IFF2 with IFF3.

The 2nd Tg shift effect is marginal. The failure surface is open and indicates that failure of a dense material under hydrostatic compression (diagonal line) will not take place (physics).

5.9. Test Case 9, laminate E-glass/MY750 epoxy , $\{\hat{\sigma}\} = (-100MPa,\ \hat{\sigma}_y,\ -100MPa,\ 0,\ 0,\ 0)^T$

Figure 13 shows the predictions of the in-plane failure strains of the multi-directional laminate at constant bi-axial compressive loading (x-z plane) with a growing loading $\hat{\sigma}_y$ in the y direction. The chosen load path leads from the interaction failure IFF2 combined with IFF3 to the same interaction failure at the lower branch of Fig.8.

5.10. Test Case 10, laminate IM7/8551-7, $\{\hat{\sigma}\} = (0,\ 0,\ \sigma_z,\ 0,\ 0,\ 0)^T$

This case was not executed with respect to the available time of the author.

5.11. Test Case 11, laminate IM7/8551-7, $\{\hat{\sigma}\} = (0,\ 0,\ \sigma_z,\ \hat{\tau}_{zy},\ 0,\ 0)^T$

The compression loading causes – due to the Poisson effect - incompatible deformations of the individual laminae. In order to achieve a bonded laminate, internal in-plane and out-of-plane shear and normal stresses are built up over the laminate thickness. A non-linear laminate analysis helps to indicate the desired critical location where the failure is initiated. There should dominate a low stress gradient in view of the high objective: Validation of a failure condition. Initial failure occurs in that critical lamina where the superposition of the shear stress with the normal stresses takes the highest stress effort. In Figure 15, the marked internal

element represents a location with a pretty low stress gradient where the material has to counteract the two loadings shear and compression.

The assumed Iosipescu test (ARCAN test rig) matches the stress situation of the task. The critical cross section is indicated in the sketch added to Figure 15. The applied external stress τ_{zy} generates different shear stresses in each of the plies. It causes a τ_{23} lamina shear stress in the 90° laminae and a τ_{31} shear stress in the 0° laminae. Due to the constant stiffness over the width (y coordinate) of the laminate specimen the τ_{zy} shear stress distributions τ_{23}, τ_{31} are parabolic according to the indicated τ_{zy} distribution. The moment of the applied shear forces F within an Iosipescu test apparatus is marginal.

The curing stress σ_2^t acts in-plane. Therefore, at the τ_{23} axis ($\sigma_z = -p = 0$) two material stress efforts are generated by τ_{23} with σ_2^t. The combined stress effort $Eff = 1$ determines the failure limit of τ_{23}. This interaction points out the start of the transition zone, IFF1 to IFF2.

On the positive σ_z axis, the tensile stress delivers a σ_3^t stress which together with the σ_2^t curing stress builds up a multi-fold failure situation. According to Equation17 the common fracture point may be estimated by $R_\perp^{tt} \approx R_\perp^t / \sqrt[m]{2} = 73/\sqrt[m]{2} \approx 57$ MPa, but this reduced strength value cannot become 'active' because σ_2^t is much smaller than σ_3^t.

Essential results:

* Shear capacity is firstly increased (IFF1 level lowered) when applying a surface pressure *p* and then decreased because IFF2 becomes the failure driving mode for higher pressures.

* Both the shear stresses were commonly checked which will be the failure driving one. The outcome of this investigation was: The 90° lamina is the critical lamina indicated by the shear stress τ_{23}.

* For $\max \sigma_z^t \rightarrow \sigma_3^t$ an IFF1-based delamination fracture occurs with separation of the laminae.

* Uni-axial wedge failure IFF2 ($Eff^{\perp\tau} = 1$) occurs if an isolated lamina is loaded up to $\sigma_z = \sigma_\perp^c = -185\ MPa$ ('isolated' strength value). However, due to the beneficial multi-axial compression the maximum stress effort $Eff^{\perp\tau}(\sigma_{eq}^{\perp\sigma}, \sigma_{eq}^{\perp\tau}) = 1$ will be firstly reached at $\sigma_z \approx -450\ MPa$ ($\varepsilon_z = -6\%$). The compressive constraining of the tensioned fibre network leads to a higher load-carrying capacity in comparison to a uni-axial compressive stress applied only.

* Reason for the low strength capacity of the laminate under pure through-thickness shear stress τ_{zy} is τ_{23} which causes IFF1 in the 90° lamina (delamination fracture, σ_3^t) and decreasingly stimulates wedge failure IFF2 for higher pressures.

* A benign IFF2 failure is caused at the y-ends due to the fact that the pressure head loading does not allow a wedge failure in contrast to "outer pressure at a free surface". A critical (catastrophic) IFF2 would be just possible at the compressed y ends of the specimen. At the free surface of the edges shear micro-cracking may occur.

*The failure curve does not run for $p = 0$ through $R_\perp^t$ on the y-axis due to the fact that τ_{23} has a compressive component (contribution to IFF2) and a tensile component (to IFF1) which interact with σ_3.

* According to the distribution of the applied shear stress the given results just stand for a local initiation of failure as onset of IFF. Naturally, there is some 'quasi-plastic' reserve (analogous to Neuber's notch theory) for the laminate when considering the τ distribution. The lower loaded vicinity around the specimen centre may take over a little loading after the onset of the central IFF1-caused degradation. Therefore, the specimen will not directly fail when reaching $\max \tau_{23}(p)$ or in other words will not be 'scissored'.

* A practical and operational end of the laminate's structural capability wrt serviceability, fitness for further use, or limit of usability is reached when the filaments directly become pressed on another. This level is reached far beyond the -450 MPa where the level of the filament tensile effort (FF1) is still not high. Hence, the laminate may be compressed higher and higher. But functionality ends with the disruption of the laminate structure. One can load the squeezed disrupted laminate again, but significant functional properties such as heat transfer might have strongly changed. The state of stresses in 90° lamina and 0° lamina are $\{\sigma\} = (185,\ -185,\ -450,\ \tau_{23} = 0,\ 0,\ 0)^T$ and $\{\sigma\} = (185,\ -185,\ -450,\ 0,\ \tau_{31} = 0,\ 0)^T$ MPa.

* FF1 will be reached about -2000 MPa. No clear value for this final failure point 'squeezing' can be given. However, this level is not of interest in normal industrial design.

5.12. Test Case 12, laminate IM7/8551-7, $\{\hat{\sigma}\} = (0,\ 0,\ \sigma_z,\ 0,\ 0,\ 0)^T$

It considers the softening curve part, the equivalent stress (considers the 'helpful' effect of multi-axial compression in comparison to uni-axial compression), the smeared stresses, and the effective pressure in the matrix material (suffix I means lamina I). All these quantities affect the degradation function η. As a simple engineering prediction - due to missing

knowledge – the stiffness-dedicated f_{2ndTg} factor is also fully used to down-scale the failure stress (≡ strength) $\sigma_z = -p$. The utilized formulas read for the TC12 material:

$$E_{sec} == \frac{E_{\perp}}{1 + 0.002 \cdot \frac{E_{\perp}}{R_{p0.2}} \cdot (\frac{\sigma_{eq}^{\perp\tau} \cdot \eta}{R_{p0.2}})^{n-1}} \qquad \text{with} \qquad \eta = \frac{1}{1 + exp(\frac{-5.78 + \varepsilon}{0.56})} ,$$

$$\sigma_{eq}^{\perp\tau} = (b_{\perp}^{\tau} - 1) \cdot (\sigma_2 + \sigma_3) \; + \; b_{\perp}^{\tau} \cdot \sqrt{\sigma_2{}^2 - 2 \cdot \sigma_2 \cdot \sigma_3 + \sigma_3{}^2 + 0} ,$$

$$\{\sigma_{m,l}\} = (\sigma_{m,1},\ \sigma_{m,2},\ \sigma_{m,3})^T = (\frac{\varepsilon_x \cdot E_p \cdot V_f) \cdot V_f}{1 - V_f},\ \sigma_{2,I},\ \sigma_z)^T \text{ and } \sigma_{ef} = \sum_{l=1}^{3} \sigma_{m,l} / 3 ,$$

$$f_{2ndTg} = 1 / \sqrt[22]{1 + \left(\frac{1 + 0.0018 \cdot \sigma_{ef}}{1.20 + 0.00092 \cdot \sigma_{ef}} \right)^{22}} .$$

Essential results:

* The results are shown in Figure 16.

* If there is no mechanical pressure head in the case of hydrostatic pressure the outer layers experience a higher wedge failure risk. However, under the given boundary conditions, the indicated wedge failure is not a hazardous one but a benign one. The load carrying capacity of the squeezed material is not exhausted for further higher loading than -450 MPa but an applicability of the laminate for further down- and up-loadings is not given anymore. So, in the frame of the assumptions there is no termination of the curve before FF1 occurs at about a filament failure strain of $\varepsilon_1^t = 1.5\%$ at $\hat{\varepsilon}_z > -15\%$. A practical and operational end of the structural capability of the laminate is reached when the filaments directly become pressed on another. The filaments become squeezed and bent and the damaged laminate cannot endure one more loading (practical maximum fibre package is about 85%, but it cannot be fully used due to non-ideal filament distribution). No clear value for a final failure point for ‘squeezing’ or ‘crushing’ can be given. See TC11, too.

6 Conclusions

-The FMC model has been successfully used to predict the failure of a polymeric material, unidirectional lamina and multi-directional laminates under a wide range of 3D stresses.

-For 3D stress analysis, a maximum of three 'modes' of the FMC model may interact

-Both failure envelopes and nonlinear stress strain curves were predicted.

-The effects of hydrostatic pressure and 2^{nd} glassy temperature were considered in the model. It was found that the 2^{nd} glassy temperature effect was minimal in all the multi-directional laminates (Test Cases 8-12).

-A number of assumptions had to be made in order to carry out the analysis. These included the interaction exponent, friction parameter, pressure dependency factor and others. It is hoped that, once the experimental results are made available, these assumptions will be re-visited.

-It was noted that some of the input data exhibited some inconsistency and these may affect the prediction of the results.

- It is worth pointing out that the theoretical predictions from the current FMC model will be compared in Ref[8] with those from other eleven methods that were employed in the WWFE-II and with test data in Part B of the WWFE-II..

Acknowledgement:

The author, who retired from industry some years ago, would like to acknowledge the help and assistance made by Dipl.-Ing. A. Freund (Institute of Lightweight Structures and Polymer Technology, TU Dresden) for computer programming. The author would also like to thank Dr.-Ing. G. Ernst from TU-Hannover, Dipl.-Ing. S. Müller (TU-Chemnitz), with CADFEM (Drs. Hoermann, Fritsch) and ANSYS (Dr. Kracht).

References

1. Hinton, M.J., Kaddour, A.S. and Soden, P.D. (2002). A comparison of the predictive capabilities of current failure theories for composite laminated, judged against experimental evidence. Composites Science and Technology, **62**: 1725-97
2. Hinton, M.J., Soden, P.D. and Kaddour, A.S. (2004). Failure criteria of fibre reinforced polymer composites. The World-Wide Failure Exercise. Elsevier, 2004, ISBN 0-08-044475-X.
3. Cuntze R.G. and Freund A (2004). the predictive capability of failure mode concept-based strength criteria for multidirectional laminates. Part A. Composites Science and Technology, **64**: 343-377
4. Cuntze R.G. (2004). The predictive capability of failure mode concept-based strength criteria for multidirectional laminates. Part B. Composites Science and Technology, **63**: 487-516
5. Cuntze R.G.(2004). Should we consider matrix yielding when investigating the deformation behaviour? 9th European-Japanese Symposium on Composite Materials. Technical University Hamburg/Harburg, May 2004
6. Cuntze, R.G. (2006). Efficient 3D and 2D Failure Conditions for UD Laminae and their Application within the Verification of the Laminate Design. Composites Science and Technology, 66 1081-1096
7. Kaddour, A.S. and Hinton, M.J. (2011). Input data for Test Cases used in benchmarking triaxial failure theories of composites. to be published in this issue.
8. Kaddour A. S. and Hinton M. J. (2012). Benchmarking of triaxial failure criteria for composite laminates: Comparison between models of 'Part (A)' of 'WWFE-II'. to be published in this issue.
9. VDI 2014 (2006). German Guideline, Sheet 3 "Development of Fibre-Reinforced Plastic Components, Analysis". (in German and English. Beuth Verlag, 2006)
10. Boehler, J.P. (1985). Failure Criteria for glass-fibre reinforced composites under confining pressure. J. Struct. Mechanics, **13**: 371.
11. Hashin Z. (1980). Failure Criteria for Unidirectional Fibre Composites. J. of Appl. Mech. **47** : 329-334
12. Awaji, H. and Sato, S. (1978). A statistical theory for the fracture of brittle solids under multi-axial stresses. Int. Journal Fracture. **14**: R13-16
13. Birch, R. (1938). The effect of pressure upon the elastic parameters of isotropic solids, according to murnaaghan's theory of finite strains. Journal of Applied Physics **9** (4): 279-288.
14. Pae, K.D. (1977). The macroscopic yielding behaviour of polymers in multi-axial stress fields. J. Mater Sci, **12**, 1209-1214
15. Pae, K.D. (1996). Influence of hydrostatic pressure on the mechanical behaviour and properties of uni-directional, laminated, graphite fibre/epoxy matrix, thick composites. Composites Part B, **27B**: 599-611
16. Srinavasta A.K. and White, J.R. (1983). Curing stresses in an epoxy polymer. J. of Applied Polymer Science. **29**, issue 6:2155-2161
17. Schneermann, M.W. and Stenzenberger, H.D. (1978). Final Report for a Study on evaluation of Built-in stresses during Manufacture of Elements made of Carbon Fibre Reinforced Plastics. Dornier System GmbH, 1978. ESTEC-Contract No. 2930/76/NL/PP(SC)
18. Shin, E.S. and Pae, K.D. (1992). Effects of hydrostatic pressure on the torsional shear behaviour of graphite/epoxy composite. Journal of Composite Materials, **28** : 462-485
19. Shin, E.S. and Pae, K.D. (1992). Effects of hydrostatic pressure on in-plane shear properties of graphite-epoxy composites. J. of Composite Materials, **26**: 828-868

20. Theriault, R., Osswald, T.A. and Stradins, L.: Properties of thermosetting polymers during cure.
21. Knops, M. (2003). Sukzessives Bruchgeschehen in Faserverbundlaminaten. Dissertation 2003. Aachen, Institut für Kunststoffverarbeitung
22. Cuntze, R.G. (2008). Strength failure conditions of the various structural materials: is there some common basis existing?, SDHM, **074:** 1-19.
23. de Boer, R. and Dresenkamp, H.T. (1989). Constitutive Equations for concrete in failure state. J. Eng. **115**: 1591-1608.
24. Beltrami, E. (1885). Sulle Condizioni di Resistenza dei Corpi Elastici. Rend. ist. d. sci. lett., Cl. mat. nat.18, 705-714 (1885).
25. Hoppel, C.R.R., Bogetti, T.A. and Gillespie, J.W.jr. (1995). Literature review – Effects of hydrostatic pressure on the Mechanical Behaviour of Composite Materials. J. of Thermoplastic Composite Materials, **8**: 375-409.
26. Hine, P.J., Duckett, R.A., Kaddour, A.S., Hinton, M.J., and Wells, G.M. (2005). The effect of hydrostatic pressure on the mechanical properties of glass fibre/epoxy unidirectional composites. Composites Part A, 279-289.
27. Cuntze, R.G. (1993). Deterministic and probabilistic prediction of the distribution of inter-fibre failure test data of pre-strained cfrp tubes composed of thin layers and loaded by radial pressure. (comparison to test results) Wollongong. Advanced Composites '93, pp. 579-585. The Minerals, Metals & Materials Society, 1993.
28. Camanho, P., Davila, C.G., Pinho, S.T., Ianucci, L. and Robinson.P. (2006). Prediction of in-situ strengths and matrix cracking in composites under transverse tension and in-plane shear. Composites, Part A **37**:165-176.
29. Puck A. and Schuermann H. (2002). Failure Analysis of FRP Laminates by Means of Physically based Phenomenological Models. Composites Science and Technology, **62:** 1633-1662.
30. Cuntze, R.G. et al. Neue Bruchkriterien und Festig-keitsnachweise für uni-direktionalen Faserkunststoffverbund unter mehrachsiger Beanspruchung –Modellbildung und Experimente. VDI-Fortschrittbericht, Reihe 5, Nr. 506 (1997).

Annex I: Determination of the UD friction parameters by experiment

A.1 Similarity betwen FMC formulations and Mohr-Coulomb formulations

The linear Mohr-Coulomb (M-C) formulation for a UD lamina may be written as

$$\overline{R}_{\tau} = \tau_n + \mu \cdot \sigma_n \qquad \text{or} \qquad \tau_n = \overline{R}_{\tau} - \mu \cdot \sigma_n \ . \tag{A1}$$

μ is an internal friction property of the UD material (usually termed friction coefficient) and $\overline{R}_{\tau}$ is the cohesion strength, corresponding to fracture plane resistance in Ref[29]. The nonlinear M-C formulations are given as

$$\tau_{nt}^{\ 2} = \overline{R}_{\tau}^{parab} \cdot (\overline{R}_{\tau}^{parab} - \mu^{parab} \cdot \sigma_n) .$$

A.2 Relationship between the FMC friction parameters and Mohr-Coulomb

A.2.1 In-plane shear $\tau_{n1}(\sigma_n)$ IFF3

For jn-plane (2D) stresses, Equation (14e) gives a nonlinear M-C relationship between the direct stress σ_n and the shear stress τ_{n1} as the following equation: $(\tau_{n1}, \sigma_n) \equiv (\tau_{21}, \sigma_2$ is valid. To avoid the complexity of solving that relationship, a simple equation was reported in Ref[6]

$$\left|\tau_{21}\right| = \overline{R}_{\perp\|} - \mu_{\perp\|} \cdot \sigma_2 . \tag{A2}$$

Due to $\sigma_n = \sigma_2$, the fracture angle is $\Theta_{fp}^{\circ} = 0$, it can be concluded from **Fig. A1**, that the cohesion strength equates the shear strength, $\overline{R}_{\tau}^{\perp\|} = \overline{R}_{\perp\|}$. The property $\mu_{\perp\|}$ is determined like $b_{\perp\|}$ from a curve fit of the IFF3 test data.

A.2.2 Transverse shear $\tau_{nt}(\sigma_n)$ IFF2

Here, the unknown angle is $\Theta_{fp}^{c} > 45°$. Following **Fig. A2,** Mohr-Coulomb formulation may be written as:

$$\tau_{nt} = \overline{R}_{\tau}^{\perp\perp} - \mu_{\perp\perp} \cdot \sigma_n . \tag{A3}$$

Transferring the FMC formulation, Equation (A3), into a Mohr-Coulomb formulation, is to express the invariants not any more in lamina stresses but in corresponding Mohr stresses, Equations (14d, 6d),

$$b_{\perp}^{\tau} \cdot \sqrt{(\sigma_n - \sigma_t)^2 + 4\tau_{nt}^2} + (b_{\perp}^{\tau} - 1) \cdot (\sigma_n + \sigma_t) = \overline{R}_{\perp}^{c} . \tag{A4}$$

Above formulation involves the still mentioned stress σ_t which cannot be representative for a Mohr envelope curve. However, despite taking this as a presumption one has nevertheless to prove that σ_t comes out of the equation when inserting apparent stress boundary conditions into the former equation. These conditions are the strength points. A further necessary condition when transferring the FMC formulation into a Mohr one is that the slope of Mohr's circle must be equal to the slope of Mohr's envelope curve in the common touching point.

The transformation of the lamina stresses into Mohr stresses depicts Fig.A2. Assuming τ_{23} = 0, which does not confine the generality because otherwise the principal stresses σ_i^{pr} can be taken, the transformation, [29]

$$\begin{bmatrix}\sigma_1\\ \sigma_n\\ \sigma_t\\ \tau_{nt}\\ \tau_{tl}\\ \tau_{nl}\end{bmatrix}=\begin{bmatrix}1 & 0 & 0 & 0 & 0 & 0\\ 0 & c^2 & s^2 & 2sc & 0 & 0\\ 0 & s^2 & c^2 & -2sc & 0 & 0\\ 0 & -sc & sc & (c^2-s^2) & 0 & 0\\ 0 & 0 & 0 & 0 & c & -s\\ 0 & 0 & 0 & 0 & s & c\end{bmatrix}\begin{bmatrix}\sigma_1\\ \sigma_2\\ \sigma_3\\ \tau_{23}\\ \tau_{31}\\ \tau_{21}\end{bmatrix} \qquad \begin{aligned}&\Theta_{fp}=\Theta_{fp}{}^{\circ}\cdot\pi/180^{\circ}\\ &c=\cos(\Theta_{fp}),\\ &s=\sin(\Theta_{fp}),\\ &C=\cos(2\Theta_{fp})=c^2-s^2\\ &S=\sin(2\Theta_{fp})=2\cdot s\cdot c\\ &C^2+S^2=1\end{aligned} \qquad \text{(A5)}$$

will lead to the relationships

$$\sigma_n=c^2\sigma_2+s^2\sigma_3\,, \qquad \sigma_t=s^2\sigma_2+c^2\sigma_3\,, \qquad \text{(A6a,b)}$$

$$\tau_{nt}=s\cdot c\cdot(-\sigma_2+\sigma_3)=s\cdot c\cdot(-\sigma)=-0.5\cdot S\cdot\sigma\,, \qquad \text{(A6c)}$$

when applying the advantageous additional theorems with Mohr stresses and when using the abbreviation $(\sigma_2-\sigma_3)=\sigma$. Mind: Mohr combines $\tau_n=\sqrt{\tau_{nt}{}^2+\tau_{n1}{}^2}$. Further holds

$$\sigma_n-\sigma_t=c^2\cdot(\sigma_2-\sigma_3)-s^2\cdot(\sigma_2-\sigma_3)=(c^2-s^2)\cdot\sigma=C\cdot\sigma\,, \qquad \text{(A7a)}$$

which is to be resolved for σ_t yielding

$$\sigma_t=\sigma_n-C\cdot\sigma\,. \qquad \text{(A7b)}$$

Then, the slope in the touching point is to be determined via the derivatives

$$d\sigma_n/d\Theta_{fp}=-2\cdot s\cdot c\cdot\sigma=-\sigma\cdot S=-\sigma\cdot\sin(2\Theta_{fp})\,, \qquad \text{(A8a)}$$

$$d\tau_{nt}/d\Theta_{fp}=-0.5\cdot 2\cdot C=-\sigma\cdot\cos(2\Theta_{fp})\,. \qquad \text{(A8b)}$$

They deliver one common equation for the slope of the envelope curve

$$d\tau_{nt}/d\sigma_n=\cot an(2\Theta_{fp})=C/S\,. \qquad \text{(A9)}$$

An implicit differentiation of the failure function $F_{\perp}^{\tau}$

$$dF/d\tau_{nt}=\frac{4b_{\perp}^{\tau}\cdot\tau_{nt}}{\sqrt{(\sigma_n-\sigma_t)^2+4\tau_{nt}{}^2}\cdot\bar{R}_{\perp}^{c}}\,, \quad dF/d\sigma_n=\frac{b_{\perp}^{\tau}-1}{\bar{R}_{\perp}^{c}}+\frac{b_{\perp}^{\tau}\cdot(\sigma_n-\sigma_t)}{\sqrt{(\sigma_n-\sigma_t)^2+4\tau_{nt}{}^2}\cdot\bar{R}_{\perp}^{c}}\,. \qquad \text{(A10a,b)}$$

*give*s the necessary analogous second equation Dividing Equation (A10b) by Equation (A10a) one obtains

$$\frac{d\tau_{nt}}{d\sigma_n} = -\frac{\frac{b_\perp^\tau - 1}{\bar{R}_\perp^c} + \frac{b_\perp^\tau \cdot (\sigma_n - \sigma_t)}{\sqrt{(\sigma_n - \sigma_t)^2 + 4\tau_{nt}^{\ 2}} \cdot \bar{R}_\perp^c}}{\frac{4b_\perp^\tau \cdot \tau_{nt}}{\sqrt{(\sigma_n - \sigma_t)^2 + 4\tau_{nt}^{\ 2}} \cdot \bar{R}_\perp^c}} \quad . \tag{A11}$$

The minus sign is due to inverse differentiation. Equating the slope equations (A9) and (A11) yields after reformulation

$$\frac{C}{S} = \frac{(b_\perp^\tau - 1) \cdot \sqrt{(\sigma_n - \sigma_t)^2 + 4\tau_{nt}^{\ 2}} + b_\perp^\tau \cdot (\sigma_n - \sigma_t)}{-4b_\perp^\tau \cdot \tau_{nt}} .$$

Into this combined equation, as the already mentioned stress boundary condition, the given fracture strength point $\sigma_2 = -\bar{R}_\perp^c = \sigma$ together with the fracture angle $\Theta_{fp} \Rightarrow \Theta_{fp}^c$ has to be inserted. This leads via the Equations (A6) and (A7) to

$\sigma_n - \sigma_t = C_{fp}^c \cdot \sigma$ and $\tau_{nt} = -0.5 \cdot S_{fp}^c \cdot \sigma$.

Finally it is obtained, when taking the negative root,

$$\frac{C_{fp}^c}{S_{fp}^c} = \frac{(b_\perp^\tau - 1) \cdot \sqrt{(C_{fp}^c \cdot \sigma)^2 + 4 \cdot (-0.5 \cdot S_{fp}^c \cdot \sigma)^2} + b_\perp^\tau \cdot (C_{fp}^c \cdot \sigma)}{-4 \cdot b_\perp^\tau \cdot (-0.5 \cdot S_{fp}^c \cdot \sigma)} = \frac{(b_\perp^\tau - 1) \cdot (-1) + b_\perp^\tau \cdot C_{fp}^c}{2 \cdot b_\perp^\tau \cdot S_{fp}^c} . \tag{A12}$$

As can be seen in the equation above: The stress σ_t has no influence. It is not representative as Mohr supposes for the Mohr envelope curve.

The final step is resolving Equation (A12) for $b_\perp^c$ which results in the relation

$$b_\perp^\tau = 1/(1 + C_{fp}^c) \qquad \text{with} \qquad C_{fp}^c = \cos\left(\frac{2 \cdot \Theta_{fp}^{c\,\circ}}{180^\circ} \cdot \pi\right) . \tag{A13}$$

A.3 Relationship between friction parameter $b_\perp^\tau$ and 'linear' Mohr-Coulomb parameters

Searching for a direct relationship between the FMC and the Mohr-Coulomb parameters requires a *comparison of coefficients* (in the strength point $\bar{R}_\perp^c$). At first Equation (A1) is employed in the shape of Equation (A3)

$$\tau_{nt} = \bar{R}_\tau^{\perp\perp} - \mu_{\perp\perp} \cdot \sigma_n \tag{A14a}$$

with $\bar{R}_\tau^{\perp\perp}$ denoting the transverse cohesive strength. Then the IFF2 failure condition Equation (A4) is applied leading to the equation

$$b_\perp^\tau \cdot \sqrt{\bar{R}_\perp^{c2} \cdot C_{fp}^{c\ 2} + 4\tau_{nt}^{\ 2}} = \bar{R}_\perp^c - (b_\perp^\tau - 1) \cdot (2\sigma_n + \bar{R}_\perp^c \cdot C_{fp}^c) . \tag{A14b}$$

In order to compare Equation (14a) with Equation (14b) both have to be firstly squared and secondly compared wrt the coefficients. This delivers

$$\bar{R}_{\tau}^{\perp\perp} = \bar{R}_{\perp}^{c} \cdot \sqrt{[(-C_{fp}^{c})^2 - 2 \cdot C_{fp}^{c} \cdot b_{\perp}^{\tau} - 2 \cdot C_{fp}^{c\,2} \cdot b_{\perp}^{\tau} + 2 \cdot C_{fp}^{c} + 1]} / (2 \cdot b_{\perp}^{\tau}) . \qquad \text{(A15a)}$$

The comparison requires the fulfilment of two conditions for the friction coefficients

$$\mu_{\perp\perp,1} = -\bar{R}_{\perp}^{c} \cdot [4 \cdot C_{fp}^{c} - 4 \cdot b_{\perp}^{\tau} + 4 \cdot b_{\perp}^{\tau\,2} \cdot C_{fp}^{c} - 8 \cdot b_{\perp}^{\tau} \cdot C_{fp}^{c} + 4] / (8 \cdot \bar{R}_{\tau} \cdot b_{\perp}^{\tau\,2}) \quad \text{and}$$

$$\mu_{\perp\perp,2} = (b_{\perp}^{\tau} - 1) / b_{\perp}^{\tau} = -C_{fp}^{c} . \qquad \text{(A15b)}$$

This means 'over determined'. The latter and simpler equation $\mu_{\perp\perp,2}$ represents a slightly smaller value and will be applied as $\mu_{\perp\perp}$.

A.4 Experimental determination of a value for the friction coefficient $\mu_{\perp\perp}$

The determination of the friction coefficient $\mu_{\perp\perp}$ is performed for the linear approach, only. From the evaluation of the test data in [30], see also **Fig. A3** and Equation (A13), the measured values $\theta_{fp}^{c}° = 55°$ ($C_{fp}^{c} = -0.342$), $\bar{R}_{\perp}^{c} = 104\ MPa$ were computed. Hence, when applying Equation (A13) it is obtained:

- FMC approach:

$$b_{\perp}^{\tau} \cdot \sqrt{I_4} = \bar{R}_{\perp}^{c} - (b_{\perp}^{\tau} - 1) \cdot I_2 ,$$

$$\Rightarrow \quad b_{\perp}^{\tau} = \frac{1}{1 + C_{fp}^{c})} = 1.52 , \quad \text{and} \quad b_{friction} = b_{\perp}^{\tau} - 1 = 0.52 ;$$

- Mohr-Coulomb approach:

$$\tau_n = \bar{R}_{\tau}^{\perp\perp} - \mu_{\perp\perp} \cdot \sigma_n ,$$

$$\Rightarrow \mu_{\perp\perp} = -C_{fp}^{c} = 0.342 , \quad \bar{R}_{\tau}^{\perp\perp} = 0.5 \cdot R_{\perp}^{c} \cdot \sqrt{C_{fp}^{c} + 1} = 36.1\ MPa .$$

Note: Assuming $\tau_{23} = 0$ is accurate for the test specimen. The determination of the material friction parameter $b_{\perp}^{\tau}$ from test generates a generally valid value.

Conclusions:

- As the matrices of the Test Cases seem to be semi-brittle as data set is proposed for the UD analyses: $\theta_{fp}^{c}° = 50°$, $b_{\perp}^{\tau} = 1.21$ or $\mu_{\perp\perp} = 0.17$, $\bar{R}_{\tau}^{\perp\perp} = 43.6\ MPa$,
- All parameter values depend on the chosen Mohr-Coulomb model (linear or parabolic or ...).

Fig. A4 eventually visualizes the received Mohr envelope curves for the in-plane and out-of-plane situation in case of the chosen linear model.

Annex II: Calculation procedure

Fig. A5 presents a flow chart of the non-linear calculation procedure. The solution procedure of the non-linear analysis aims to establish static equilibrium at each load step after material properties have been changed. When $Eff = 1$ has been reached,, this total combined stress effort value is kept

constant throughout the degradation procedure till the fibres take over above additional load. After the first IFF and after reaching $Eff = 1$ the associated mode stress effort $Eff_{crit}^{mode} = \sigma_{eq}^{mode} / R^{mode}$ is left as a decaying fracture energy portion (numerical damping) in the interaction equation. Note that σ_{eq}^{mode} decreases in the softening domain and R^{mode} is kept constant.

In areas where failure modes do interact, it is a good practice to consider the interaction between the modes in the following manner: The secant moduli E_{2sec} and G_{21sec} are taken from the $\sigma_2(\varepsilon_2)$-curves or the $\tau_{21}(\gamma_{21})$-curve not just at the stresses $\sigma_{eq}^{\perp\tau}$, $\sigma_{eq}^{\perp\sigma}$ or $\sigma_{eq}^{\perp||}$ resulting from the stress and strain analysis. Their values are taken in the 'hardening branch' at a little higher stress as follows

$$\sigma_{eq,corr}^{mode} = \sigma_{eq}^{mode} \cdot f_{trf} \tag{25a}$$

with the trigger factor for hardening

$$f_{trf} = \sqrt[m]{Eff / Eff_{crit}^{mode}}, \qquad Eff = \sqrt[m]{(Eff_{crit}^{mode})^m + \sum (Eff_{others}^{mode})^m} \tag{25b}$$

to consider a mode-combined degradation effort. By this approach slightly lower secant moduli are provided for the next calculation loop; lower than those that would result without the correction by the triggering approach. The controlling parameter is the ratio of ‘total stress effort’ *Eff* to ‘critical mode stress effort’. Naturally, this triggering approach is already active before the onset of a distinct IFF.

Once IFF has been reached, the secant modulus $E_{sec}(\sigma_{eq}^{mode})$ can be determined by applying Equation (33).

.

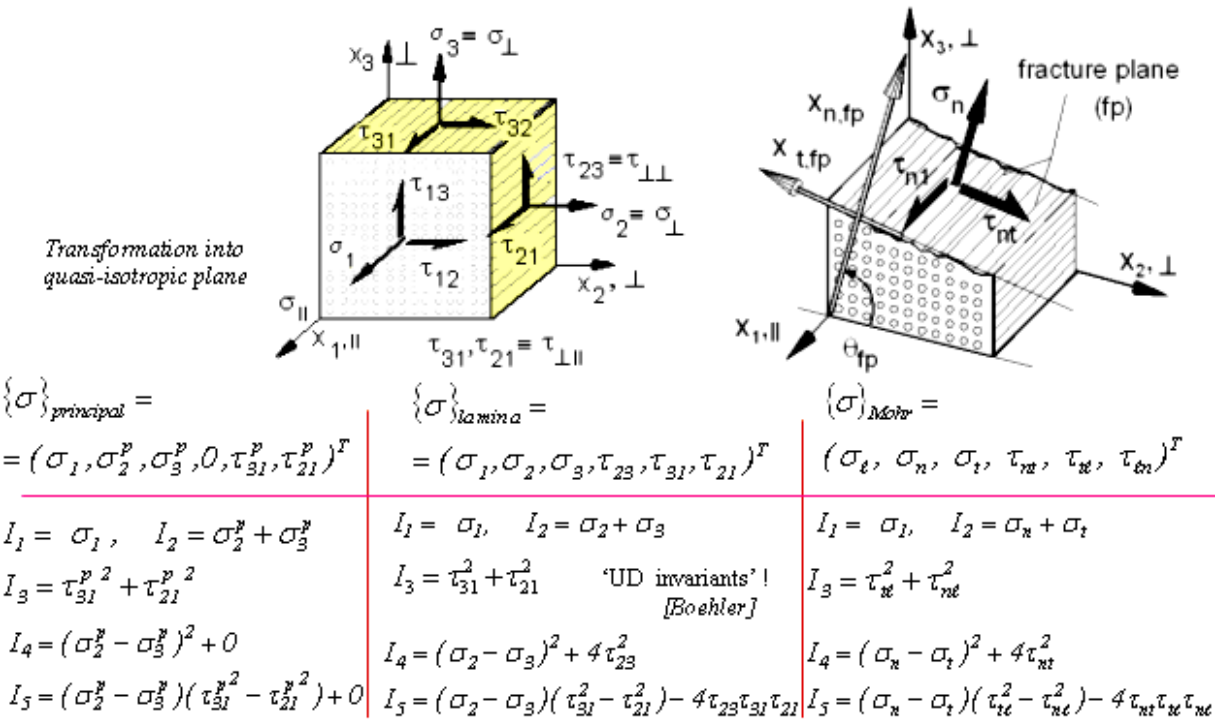

Fig. 1. Formulations of lamina stresses and invariants for UD material

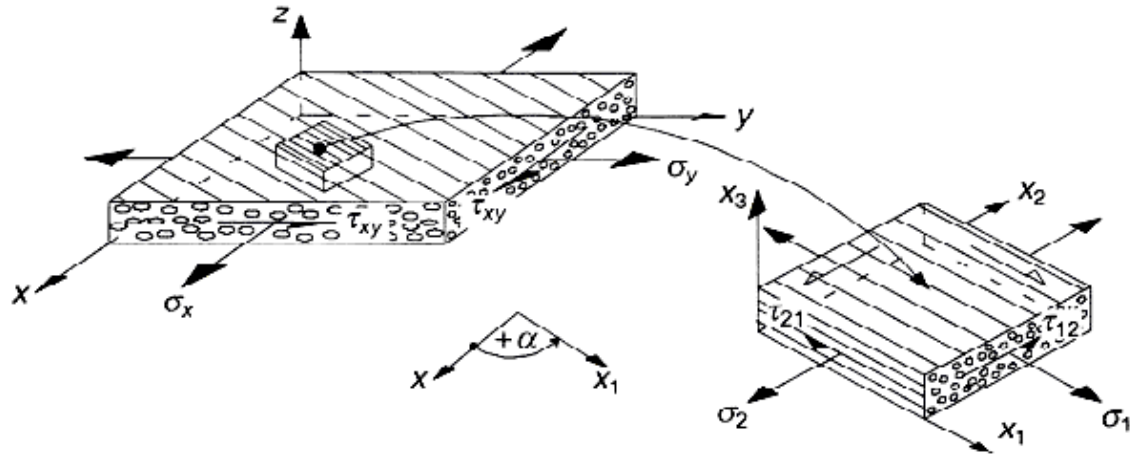

Fig. 2. In-plane lamina stresses with definition of positive fibre orientation angle of the lamina (inter-laminar stresses are not depicted here).

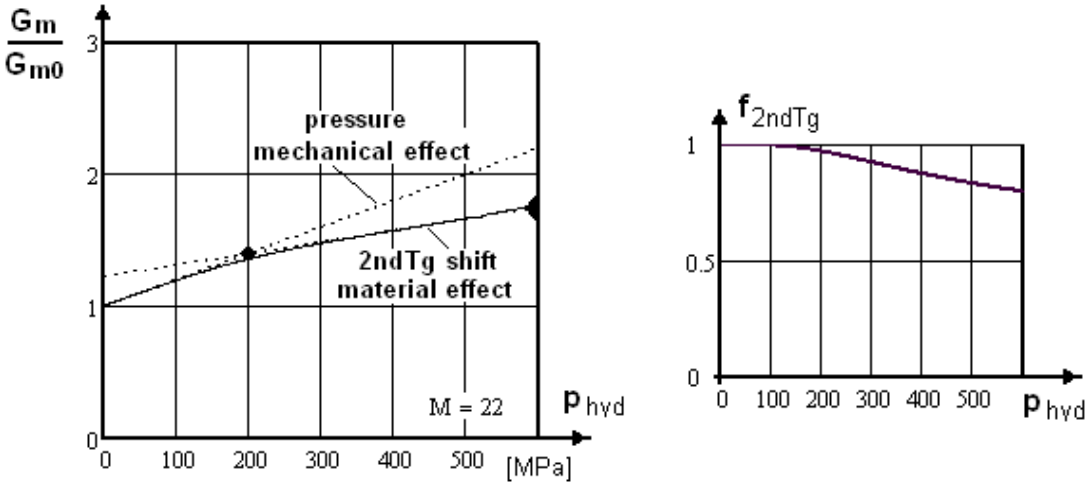

Fig. 3a. 2nd Tg shift effect: Dependence of the matrix modulus on p_{hyd}. Assumption for PR319: knee point (140 MPa at ratio 1.4), final point (600 MPa at ratio 1.75, see [15]

Fig. 3b. Decay function f_{2ndTg} due to 2ndTg shift. $M = 22$, $a_1 = 0.0018$, $a_2 = 1.20$, $a_3 = 0.00092$.

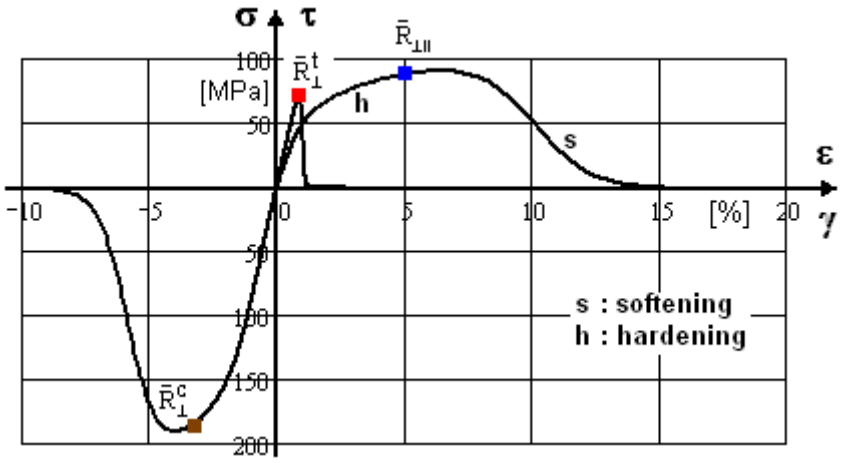

Fig. 4. IFF-related stress-strain curves of a UD-lamina with strain-hardening (isolated lamina) branch and assumed strain-softening branch (embedded lamina), see [4]

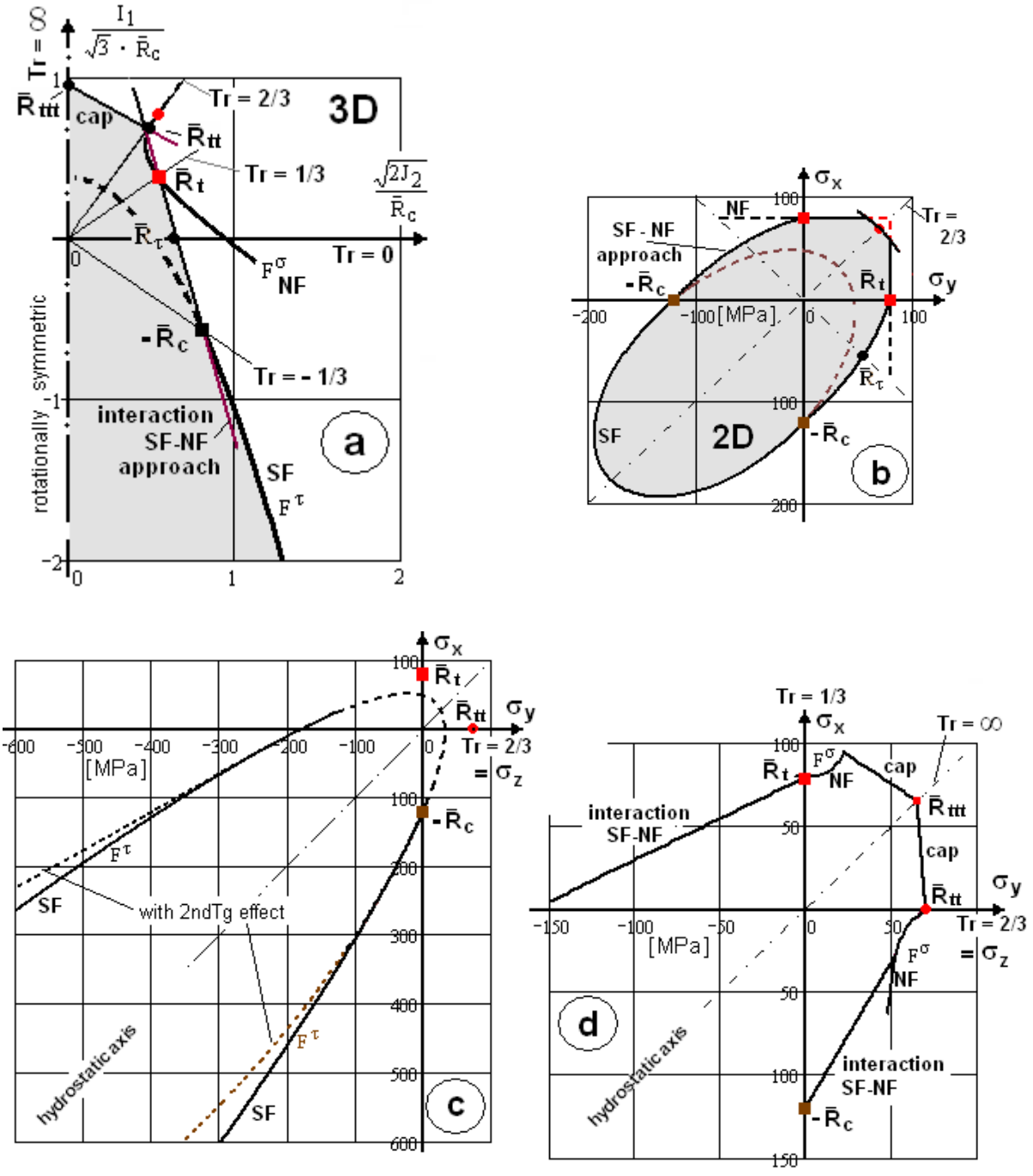

Figure 5 Tri-axial failure state of MY750 epoxy resin matrix: $\{\sigma\}=(\sigma_x,\sigma_y=\sigma_z,\sigma_z,0,0,0)^T$.
a) 3D visualization in Lode coordinates with approaches in the cap as well as the SF-NF interaction domain; b)2D failure curve. c) 3D compressive failure stress σ_x vs. stress $\sigma_y (=\sigma_z)$; d) Details of c).

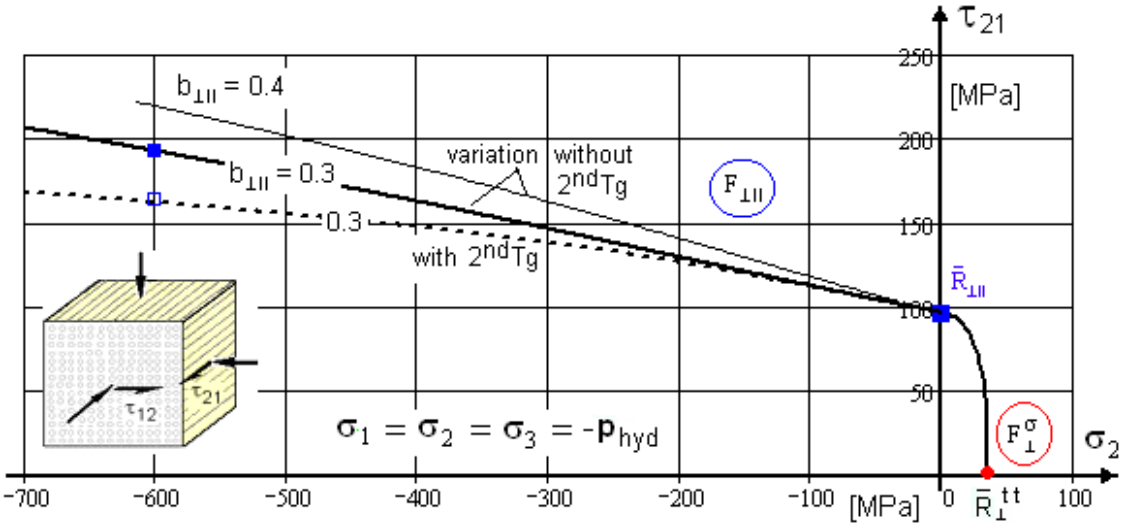

Figure 6. Fracture stress τ_{21} vs stress $\sigma_2 (= \sigma_1 = \sigma_3 = -p_{hyd})$ for a UD T300 carbon/ PR319ep

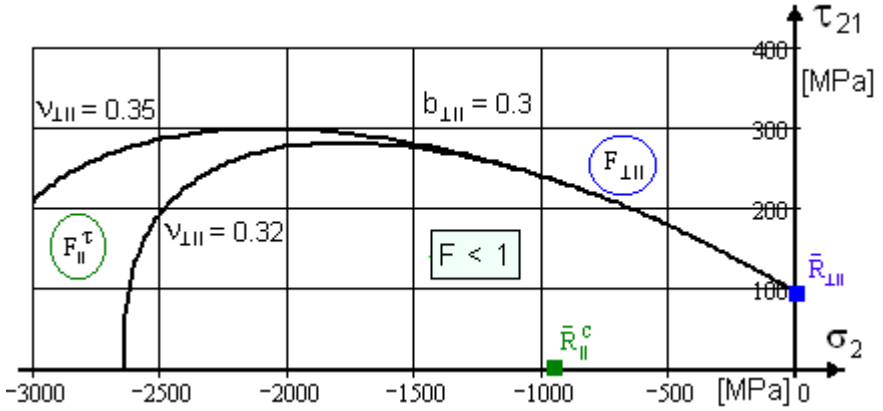

Figure 6b. Closing of the failure curve and sensitivity study on Poisson's ratio monotonically increasing with hydrostatic pressure.

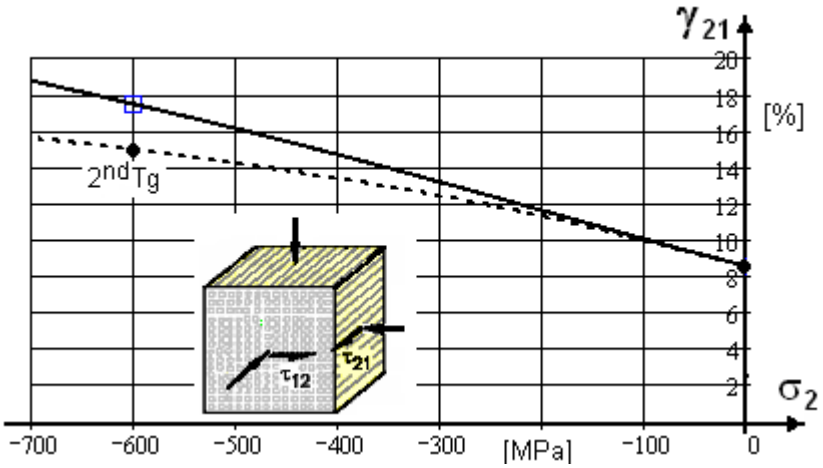

Figure 7. Failure shear strain $\gamma_{21}(\sigma_2 = -p_{hyd})$ in dependence of an increasing p_{hyd} for a UD T300 carbon/PR319 epoxy. Properties, see TC2.

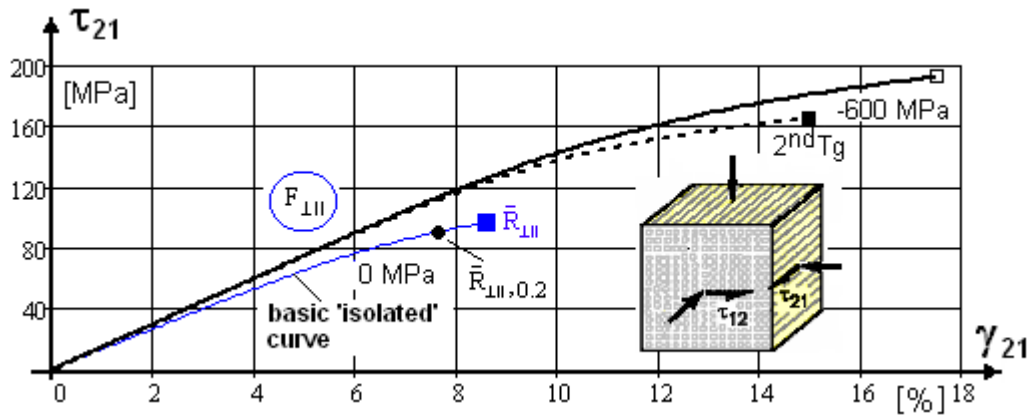

Figure 8. Shear stress- shear strain curve $\tau_{21}(\gamma_{21})$ for $\sigma_{hyd} = 0,\ -600\ MPa.$

UD T300 carbon/PR319 epoxy. Properties, see TC 2.

2^{nd}Tg shift (dashed line). $\gamma_{21}^{fr,-600} = 15\%$, $\tau_{c0.2,21}^{-600} = 125\ MPa$, $G_{12}^{-600} = 1872\ MPa$, $\tau_{21}^{fr,-600} = 193\ MPa$, $\bar{R}_{\perp\|} = 97 MPa$ ■(8.6%), $\bar{R}_{\perp\|,0.2} = 91 MPa$ ●, $\tau_{21}^{fr,-6002ndTg} = 165\ MPa$ ▪ (15%).

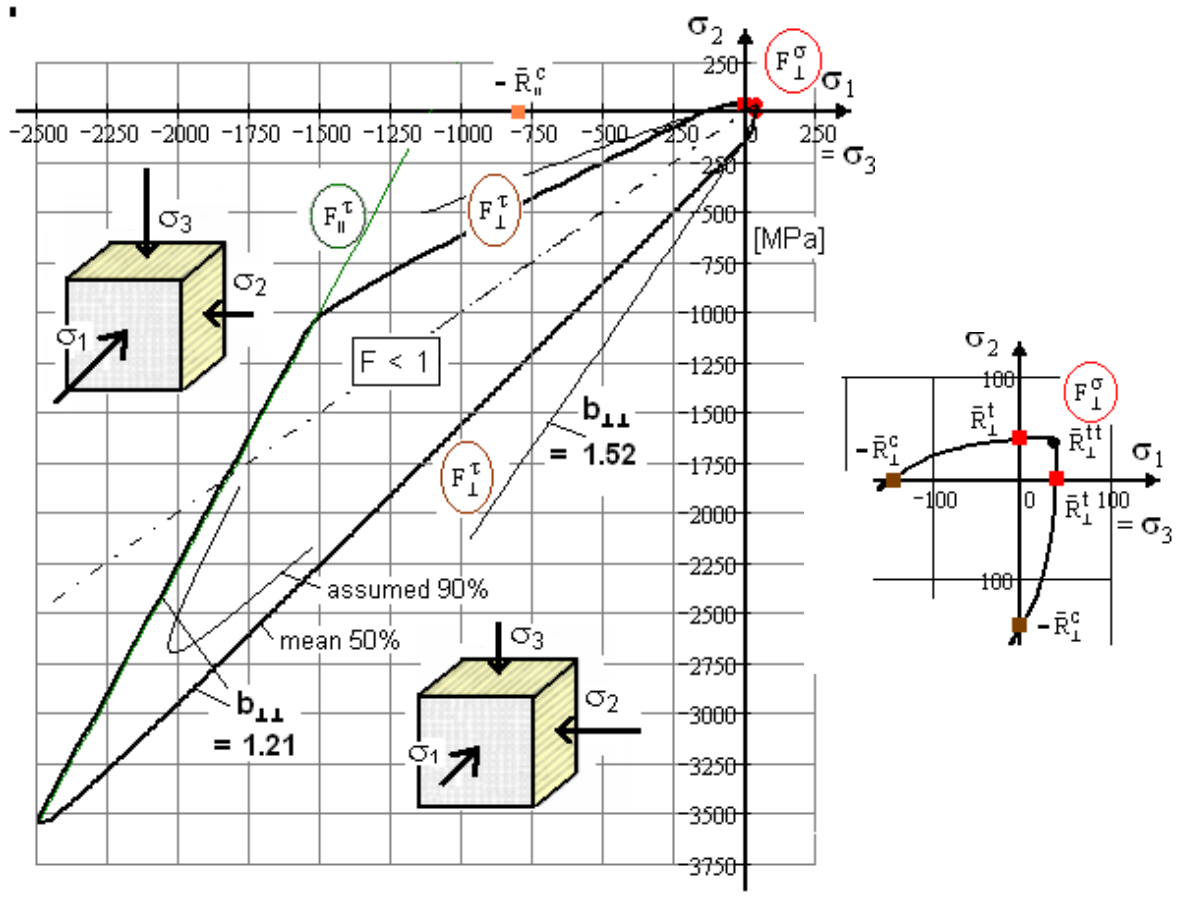

Figure 9. Tri-axial failure state of stress: σ_2 vs. longitudinal stress σ_1 $(= \sigma_3)$ for a UD E-glass/MY750epoxy.

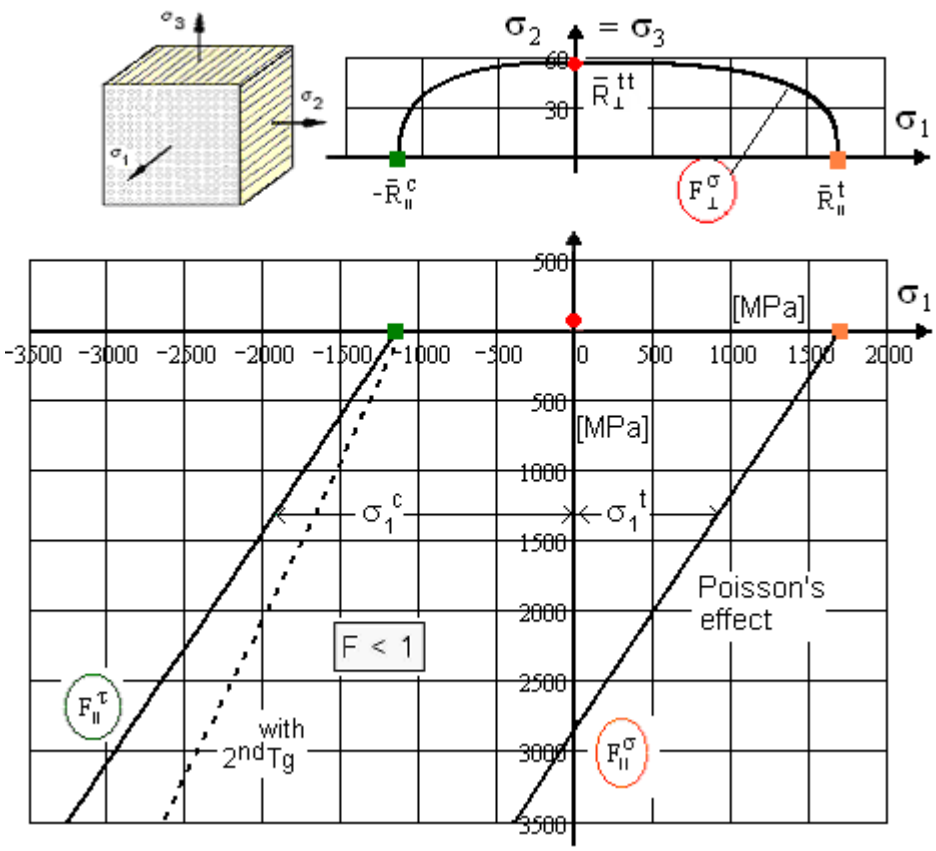

Figure 10. Through-thickness stress σ_3 *(=* σ_2*)* vs. fibre-parallel stress σ_1 , UD S-glass/epoxy2.

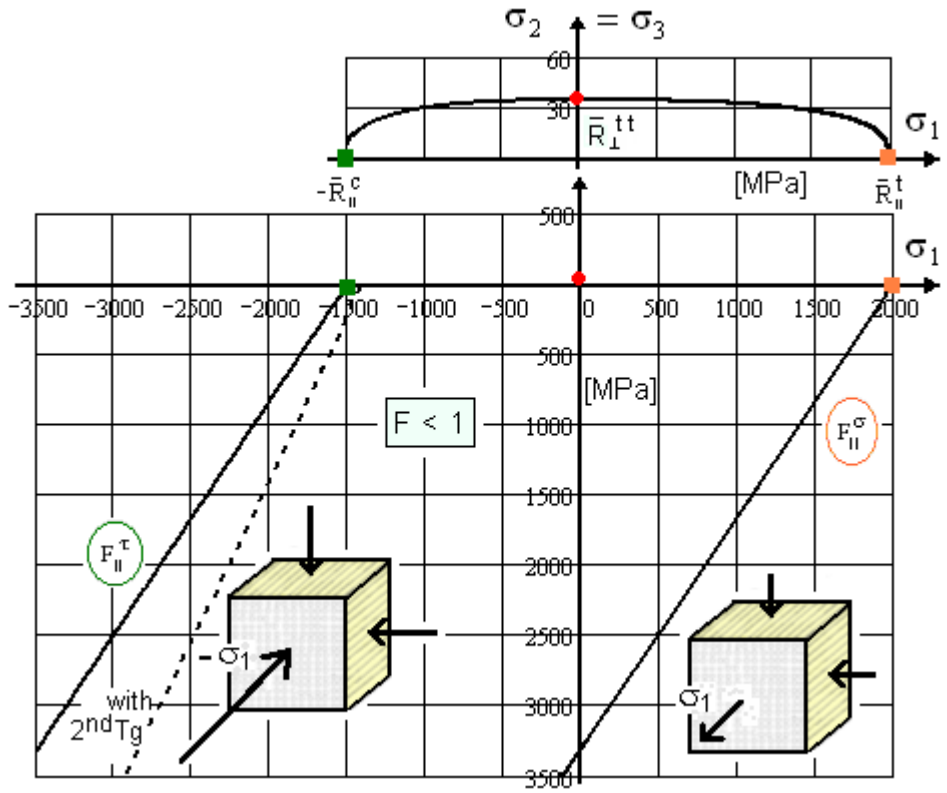

Figure 11. Through-thickness stress σ_3 (= σ_2) vs. fibre-parallel stress σ_1. UD A-S carbon/epoxy1.

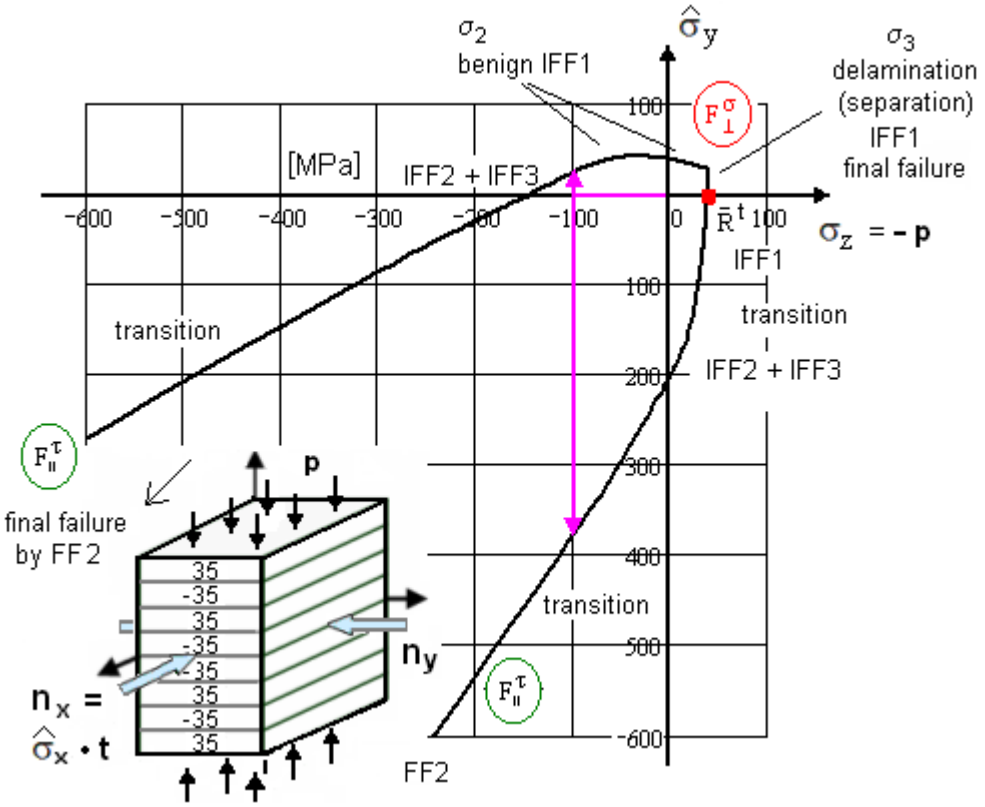

Figure 12. Effect of the applied surface pressure $\sigma_z = -p$ (through-thickness stress) on the size of the normal section force $n_y = \hat{\sigma}_y / t$ at fracture, with $n_x / t = \hat{\sigma}_x = \sigma_z$. UD lamina-composed laminate $[35/-35/35/-35]_s$, E-glass/MY750/epoxy.

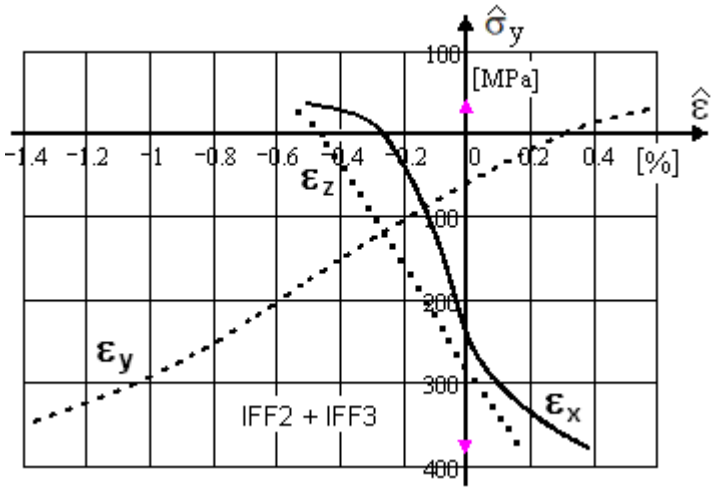

Figure 13. Stress-strain curves $\hat{\sigma}_y(\hat{\varepsilon}_x)$ and $\hat{\sigma}_y(\hat{\varepsilon}_y)$. Monotonically loaded $\hat{\sigma}_x = \hat{\sigma}_y = \sigma_z$ up to *-100MPa.* Then remain constant: $\sigma_z = \hat{\sigma}_x = -100MPa$, $\hat{\sigma}_y = n_y / t$ grows.

Figure 14. Applied section shear load-caused maximum-thickness failure shear stress τ_{zy} vs. applied through-thickness stress σ_z. for a $[45/-45/90/0]_{ns}$, IM7/8551-7. $\sigma_x = \sigma_y = 0$,

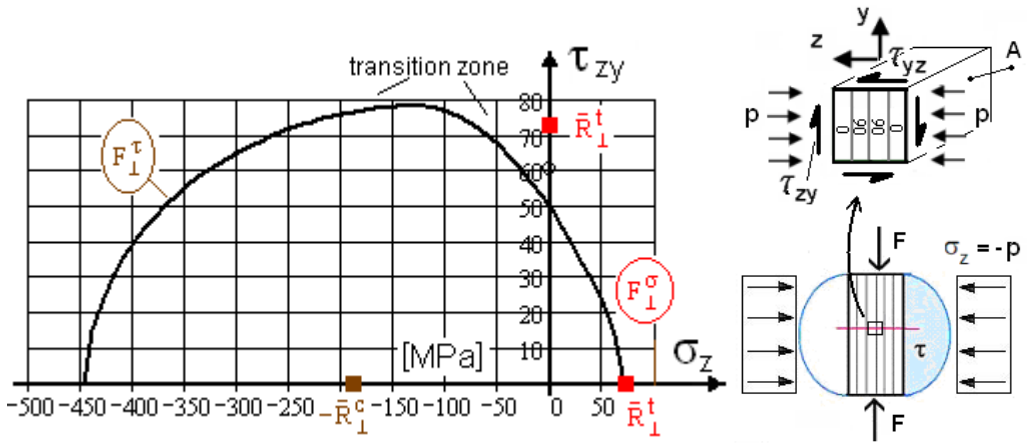

Figure 15. Thickness failure shear stress τ_{zy} vs. applied through-thickness stress σ_z. $[0/90/0/90]_{ns}$ carbon/epoxy laminate IM7/8551-7. ARCAN test rig, loaded by shear forces F and pressure p. $\max \tau_{zy} = \max \tau_{23} = \max \tau_{21} = 1.5 \cdot F / A$.

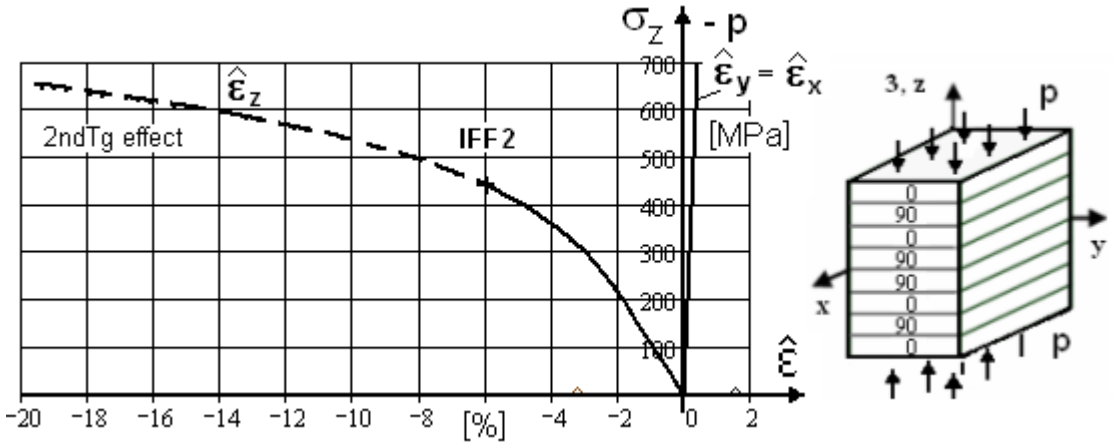

Figure 16. Stress-strain curves caused by a through-thickness compressive stress σ_z for a $[0/90/0/90]_{ns}$ carbon/epoxy laminate, carbon/epoxy laminate, IM7/8551-7. $\sigma_x = \sigma_y = 0$.

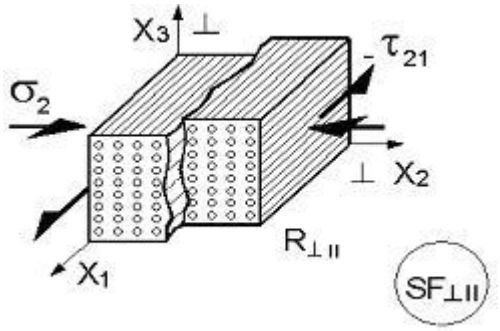

Fig. A 1. Stresses at shear failure IFF3

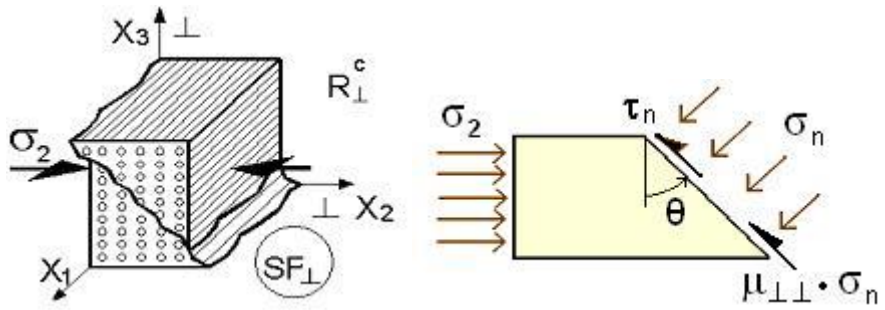

Fig.A 2. Lamina stresses and Mohr stresses at shear failure IFF2 (wedge failure).

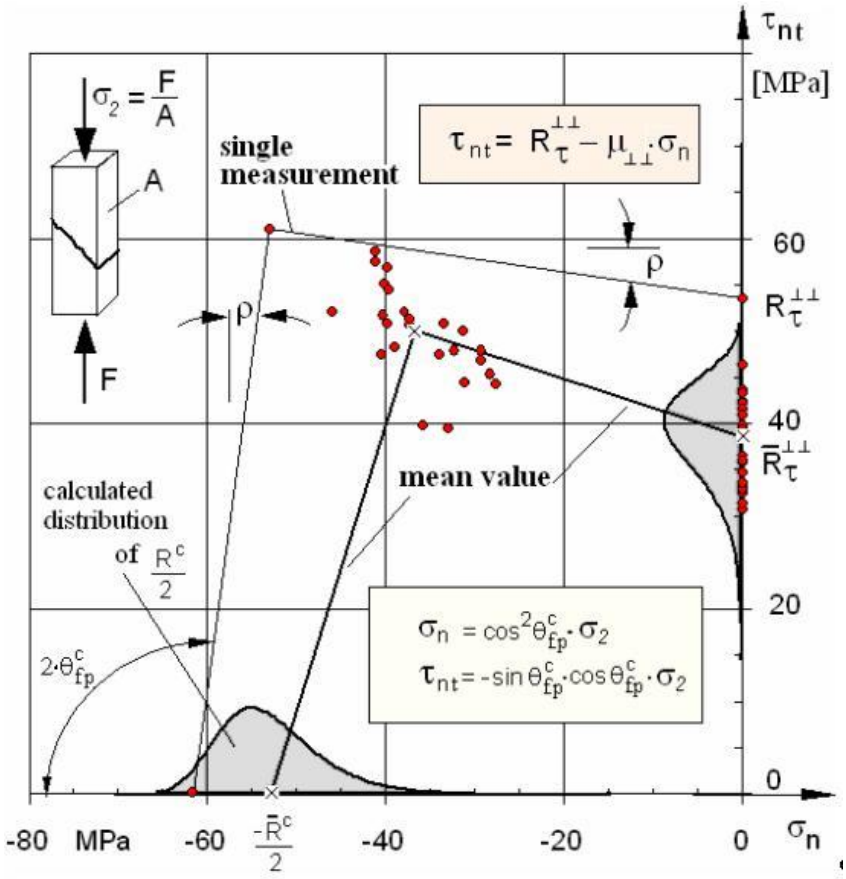

Fig. A 3. Linear IFF2 Approach and Validation by Test Data. Glass/epoxy, [30].
Friction angle: $tan\,\rho = -\mu_{\perp\perp}$

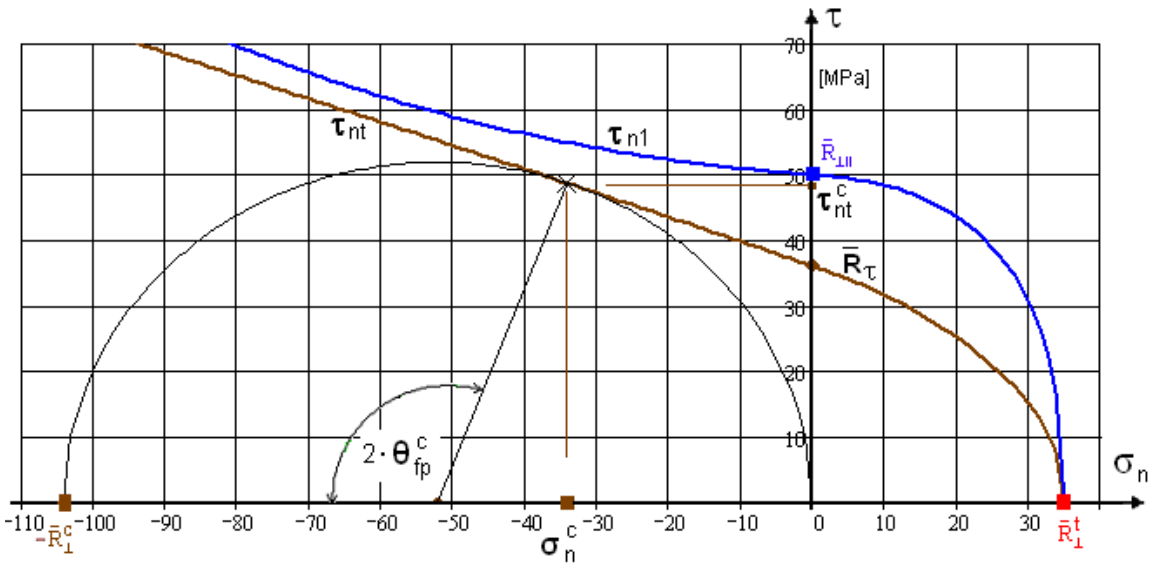

Fig. A 4. Mohr-Coulomb failure envelopes $\tau_{n1}(\sigma_n)$, $\tau_{nt}(\sigma_n)$

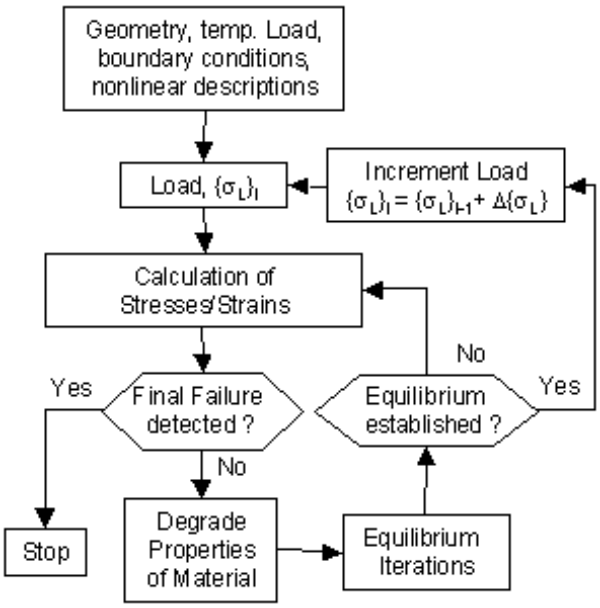

Fig. A 5. Non-linear calculation scheme of the self-correcting secant modulus method. Matrix weakening is considered in the degradation box